Chapter 5

A Robust Damping Control for Battery Energy Storage Integrated Power Systems to Mitigate Inter-Area Oscillations

5.1 Introduction

This chapter presents the effect of a Battery Energy Storage System (BESS) on the power system inter-area oscillations under changing load conditions. The dynamic interaction between the BESS control modes and synchronous generators, along with BESS control parameters, influence the damping of prominent inter-area oscillations under different loading conditions. Furthermore, H_∞ mixed sensitivity scheme-based Wide-Area Damping Controller (WADC) is proposed for BESS. This controller is designed using the Linear Matrix Inequality (LMI) framework to mitigate the prominent inter-area oscillation of the power system. Sensitivity to control parameter variation and the geometric measure of the observability are utilized to select the location and feedback signal for the WADC. The performance of the proposed WADC is compared with an Energy Storage System-based stabilizer and WADC proposed in an existing work on a modified New England ten-machine benchmark system. The Real-Time Digital Simulator (RTDS) platform is used to assess the real-time viability of the proposed WADC. The simulation results demonstrate that the proposed WADC can effectively diminish several inter-area modes.

Additionally, it offers robust performance under varying load conditions and contingencies and with communication delays in feedback signals. The proposed controller is also effective under the system integrated with Doubly Fed Induction Generator-based Wind Turbine System.

5.2 Power System Modeling

All power system components must be properly modelled to do a small-signal analysis. Each SG in this work is represented by a 6^{th}- order model and equipped with a type I governor and an IEEE type I excitation system. The conventional PSSs are chosen for local control of SG. The loads are treated as constant impedance type load models. The subsequent subsection provides the mathematical modelling for BESS and the appropriate control method.

5.2.1 Modeling of battery energy storage system

The BESS is integrated into the power network along with the associated controller, as shown in Fig. 5.1. The BESS comprises of battery pack model, Voltage Source Converter (VSC), filter, and inter-facing transformer. The dynamic model of BESS is discussed in this subsection.

5.2.1.1 Battery model

The electrical equivalent battery cell model also referred to as the two-time constant model, is presented in this work as shown in Fig. 5.2, and its parameters are dependent on the state of charge [94]. The battery cell's dynamic modeling is expressed as follows using Fig. 5.2:

$$\begin{cases} pV_1 = -\dfrac{V_1}{R_1C_1} + \dfrac{I_b}{C_1} \\ pV_2 = -\dfrac{V_2}{R_2C_2} + \dfrac{I_b}{C_2} \\ pI_b = \dfrac{1}{L}\left(V_o + I_bR_{in} + V_1 + V_2 - V_{dc}\right) \\ pV_{dc} = \left(\dfrac{I_b - I_{dc}}{C_{dc}}\right) \end{cases} \tag{5.1}$$

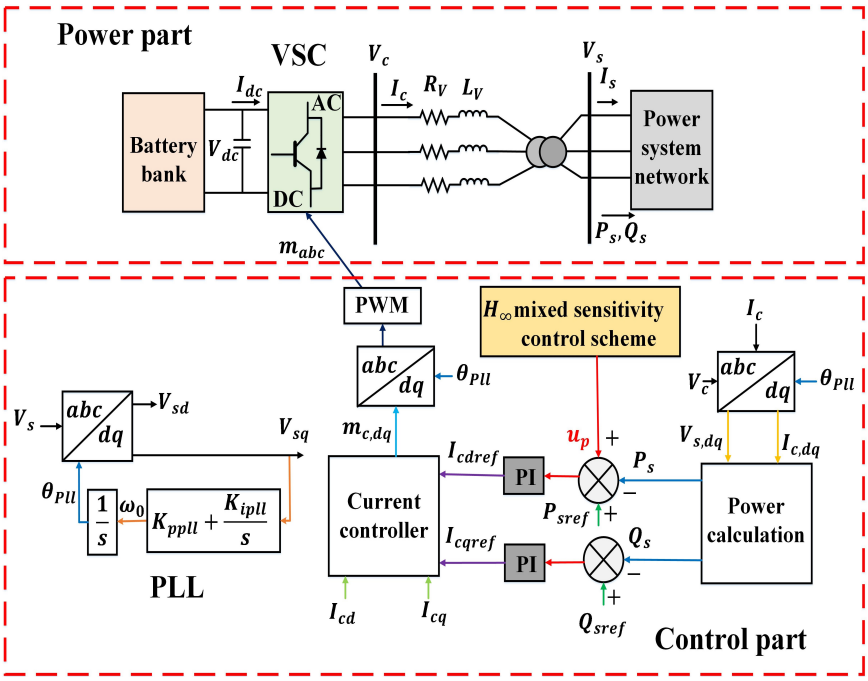

Figure 5.1: Schematic of the BESS integrated power system and associated controls.

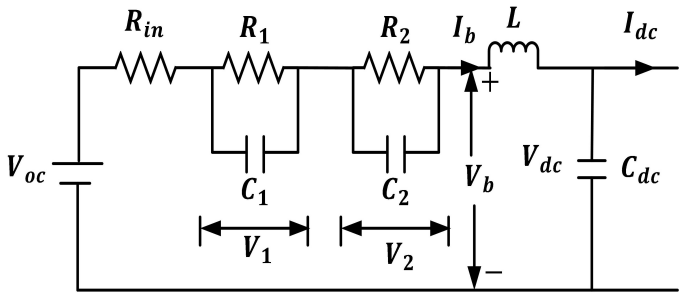

Figure 5.2: Schematic of electrical equivalent battery cell model.

where p is the differential operator, V_1 and V_2 are the voltage drops across $R_1 \,||\, C_1$ and $R_2 \,||\, C_2$, respectively; R_{in} is the charge transfer resistance; V_{oc} is the open circuit voltage; V_b is the terminal voltage of the battery cell; I_{in} is the battery pack current; C and L are the capacitance and inductance, respectively; and I_{dc}, V_{dc}, and C_{dc} are the current, voltage, and capacitor of the DC link, respectively.

5.2.1.2 Modeling of VSC

VSC model presented in Section 4.2.1.3 of chapter-4 was considered.

5.2.1.3 Primary control strategy for the BESS

The two-stage control strategy presented in Section 4.2.1.4 is used. The primary level control maintains the constant DC-link voltage (V_{dc}) and voltage level V_{sd} at the point of coupling, whereas the secondary level control adjusts the modulation index (m_{dq}) of VSC.

5.2.2 Power system model with time delay

The power system model, which includes the nonlinear model of SGs, transmission networks, loads, BESS, and related controllers, is described by differential and algebraic equations. The representation of the state-space model for the power system is described using (3.8) of chapter-3.

The linearized power system model in (3.8) is a model without time delay; however, global feedback signals are inherited with communication time delay. Therefore, the first-order Pad'e approximation[46] utilized to model the time delay (T_d) as stated in (3.9) of chapter-3.

The state-space model of the time-delay transfer function is represented using (3.10) in chapter-3.

The power system model without time delay stated in (3.8) is cascaded with a system with a time delay model in (3.10) to obtain a power system model with an output time delay model defined as (3.11) of chapter-3.

The system state, input, and output matrices of power system with time delay are represented by (3.12) of chapter-3.

5.2.2.1 Feedback loop selection for the damping controller

The relevant, prominent inter-area modes are identified using small-signal analysis of the power system linear model with time delay (3.11). This work utilizes geometric measures to choose feedback signals for the damping controller because they can assess the controller's performance in comparison to a specific mode and the relative strength of a signal. The Geometric Measurements of Observability (GMO) $gm_{oj}(k)$ associated with mode k is calculated using (2.24) of chapter-2.

The feedback signal with the highest GMO in prominent oscillation mode is chosen

to design the damping controller for the BESS integrated power system.

5.3 WADC Design Formulation: H_∞ Mixed Sensitivity Control Method

The LFOs start in the multi-machine power networks when it experiences disturbances such as load changes, a short circuit on a generator bus, and transmission line outages. Therefore, this work designed H_∞ mixed sensitivity scheme based WADC for the BESS using the Linear Matrix Inequality (LMI) approach in order to reduce these oscillations.

The WADC proposed in this work provides additional damping by producing a supplementary control signal for the BESS' active power control loop. Apart from reducing inter-area oscillations, the controller is able to achieve additional performance goals, such as control effort reduction, robustness enhancement, and disturbance rejection. These control objectives are taken as constraints for the closed-loop transfer functions, such as complementary sensitivity functions $K(s)S(s) = K(s)(I - G(s)K(s))^{-1}$, which addresses robustness concerns and reduces control effort, and the sensitivity function $S(s) = (I - G(s)K(s))^{-1}$, which validates disturbance rejection.

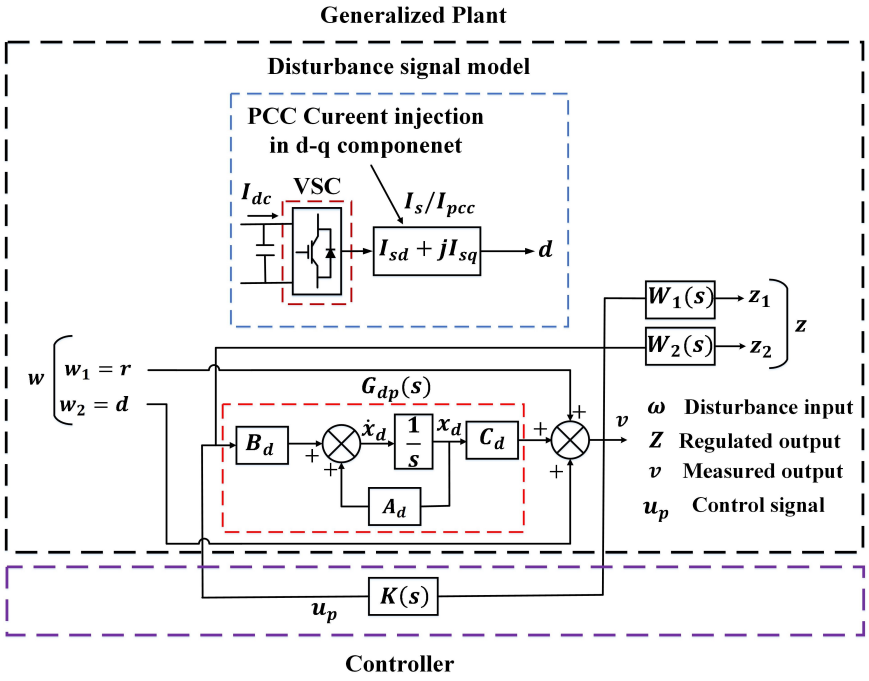

Figure 5.3: Block diagram for mixed sensitivities control with disturbance signal model.

The formulation for H_∞ mixed sensitivity control problem includes the shaping of the

$S(s)$, as well as the $K(s)S(s)$. The H_∞ mixed sensitivity control block diagram is depicted in Fig. 5.3, where $G_{dp}(s)$ represents the open loop plant, $K(s)$ represents the controller to be designed, I_{sd}, and I_{sq}, are the point of coupling current in d-q axis, d represents the disturbance signal, and $W_1(s)$ and $W_2(s)$ represent the shaping filter, respectively. $W_1(s)$ is a low pass shaping filter with a bandwidth equal to the disturbance signal selected to design the stabilizing controller that minimizes $\|W_1(s)S(s)\|_\infty$, and $W_2(s)$ is a high pass shaping filter with a crossover frequency that is almost equal to the desired bandwidth of generalized plant.

The mixed sensitivity (S/KS) control design aim is described in [90] as

$$\left\| \begin{bmatrix} W_1(s)S(s) \\ W_2(s)K(s)S(s) \end{bmatrix} \right\|_\infty < 1 \tag{5.2}$$

According to Fig. 5.3, the mixed-sensitivity control method's generalized plant P_d is obtained as

$$P_d = \begin{bmatrix} W_1 & W_1 & W_1 G_{pd} \\ 0 & 0 & W_2 \\ 0 & I & G_{pd} \end{bmatrix} = \begin{bmatrix} P_{d11} & P_{d12} \\ P_{d21} & P_{d22} \end{bmatrix} \tag{5.3}$$

so that its components resemble those of $z, v, w,$ and u_p and when placed in the generalized control configuration as,

$$\begin{cases} z = P_{d11} w + P_{d12} u_p \\ v = P_{d21} w + P_{d22} u_p \end{cases} \tag{5.4}$$

Simultaneously, the state-space formulation for the generalized plant P_d, depicted in Fig. 5.3, may be expressed as

$$\begin{cases} p x_d(t) = A_d x_d(t) + B_{d1} w(t) + B_{d2} u_d(t) \\ z(t) = C_{d1} x_d(t) + D_{d11} w(t) + D_{d12} u_d(t) \\ v(t) = C_{d2} x_d(t) + D_{d21} w(t) + D_{d22} u_d(t) \end{cases} \tag{5.5}$$

where x_d, and u_d are the state vector and input of the generalized plant, respectively; w is the disturbance input; u_p is the damping control signal; and z, and v, are the regulated outputs and measured output signals for the damping controller, respectively.

In state-space representation, the damping controller K can be written as

$$\begin{cases} px_k(t) = A_k x_k(t) + B_k v(t) \\ u_p(t) = C_k x_k(t) + D_k v(t) \end{cases} \tag{5.6}$$

where x_k is the damping controller state vector, A_k, B_k, C_k, and D_k are the damping controller system state, input, output, and feed-forward matrices, respectively.

The H_∞ mixed sensitivity control method-based WADC design is implemented to the BESS integrated power system as depicted in Fig. 5.4. In this study, the design of the damping controller considers the disturbance inputs (w) (taken as $w_1 = r = 0$ and $w_2 = d = I_s$), regulated outputs (v) (taken as ($P_{sref} - P_s$) and ($Q_{sref} - Q_s$)), measured output signals (z) (taken as active power flow through the line P_{line}), and the control signal output (u_p) linked to the active power control loop of the BESS primary controller. Further, the proposed controller output signal is associated with the d-axis reference current (I_{cdref}) of the BESS primary controller.

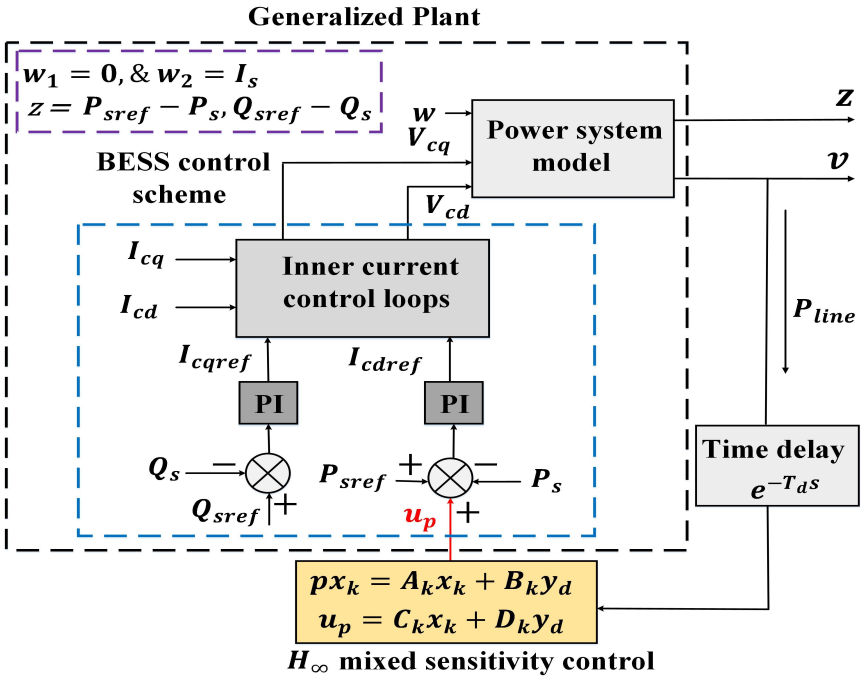

Figure 5.4: BESS damping control design strategy.

The closed-loop transfer function (M_{zw}) from the disturbance input to the regulated output is expressed as follows:

$$M_{z\omega}(s) = \begin{bmatrix} W_1(s)S(s) \\ \\ W_2(s)K(s)S(s) \end{bmatrix} = C_{cl}(SI - A_{cl})^{-1}B_{cl} + D_{cl} \tag{5.7}$$

where

$$A_{cl} = \begin{bmatrix} A_d + B_{d2} D_k C_{d2} & B_{d2} C_k \\ B_k C_{d2} & A_k \end{bmatrix}$$

$$B_{cl} = \begin{bmatrix} B_{d1} + B_{d2} D_k D_{d21} \\ B_k D_{d21} \end{bmatrix}$$

$$C_{cl} = \begin{bmatrix} C_{d1} + D_{d12} D_k C_{d2} & D_{d12} C_k \end{bmatrix}$$

$$D_{cl} = \begin{bmatrix} D_{d11} + D_{d12} D_k D_{d21} \end{bmatrix}$$

The weighted closed-loop transfer functions in (5.7) must be minimized in order to find an internally stabilizing controller. The output control synthesis is solved by Riccati equations using the LMI framework, which placed the prominent closed-loop pole inside a predetermined LMI zone. If there is the existence of an $X = X^T > 0$, where X is the real symmetric matrix, the damping control design objective is satisfied such that

$$\begin{bmatrix} A_{cl}^T X + X A_{cl} & B_{cl} & X C_{cl}^T \\ B_{cl}^T & -I & D_{cl}^T \\ C_{cl} X & D_{cl} & -I \end{bmatrix} < 0 \tag{5.8}$$

The asymptotic stability with $\|M_{z\omega}\|_\infty < 1$ is assured by the presence of $X = X^T > 0$ in (5.8). However, (5.8) includes $A_{cl}X$ and $C_{cl}X$, where A_{cl} and C_{cl} depend on damping controller parameters A_k, B_k, C_k, and D_k. The product of control variables and X introduces the nonlinearity in the controller design problem. This nonlinearity can be eliminated by modifying the controller variables. The newly defined controller variables are presented in (5.9). This modification provides a linearized framework to solve the controller design problem.

$$\begin{cases} A_{1k} = N_1 A_k M_1^T + N_1 B +_k C_{d2} R_1 + S_1 B_{d2} C_k M_1^T + \\ \qquad S_1 \left(A_d + B_{d2} D_k C_{d2} \right) R_1 \\ B_{1k} = N_1 B_k + S_1 B_{d2} D_k \\ C_{1k} = C_k M_1^T + D_k C_{d2} R_1 \\ D_{1k} = D_k \end{cases} \tag{5.9}$$

where, R_1, S_1, M_1, and N_1 are the sub-matrices of X.

The required transformation in (5.8) is achieved by substituting the new control variables from (5.9). This substitution results in the solution for the design of the damping controller problem, outlined as follows [95]:

$$\begin{bmatrix} R_1 & I \\ I & S_1 \end{bmatrix} > 0 \tag{5.10}$$

$$\begin{bmatrix} \varphi_{11} & \varphi_{21}^T \\ \varphi_{21} & \varphi_{22} \end{bmatrix} < 0 \tag{5.11}$$

where

$$\varphi_{11} = \begin{bmatrix} A_d R_1 + R_1 A_d^T + B_{2d} C_{1k} + C_{1k}^T B_{2d}^T & \varphi_{1A} \\ (B_{1d} + B_{2d} D_{1k} D_{21d})^T & I \end{bmatrix}$$

$$\varphi_{21} = \begin{bmatrix} A_{1k} + (A_d + B_{2d} D_{1k} C_{2d})^T & S_1 B_{1d} + B_{1k} D_{d21} \\ C_{1d} R_1 + D_{12d} C_{1k} & D_{11d} + D_{12d} D_{1k} D_{21d} \end{bmatrix}$$

$$\varphi_{22} = \begin{bmatrix} A_d^T S_1 + S_1 A_d + B_{1k} C_{2d} + C_{2d}^T B_{1k}^T & \varphi_{2A} \\ C_{1k} + D_{12d} D_{1k} C_{2d} & -I \end{bmatrix}$$

where, $\varphi_{1A} = B_{1d} + B_{2d} D_{1k} D_{d21} \, (B_{1d} + B_{2d} D_{1k} D_{d21})^T$

, $\varphi_{2A} = (C_{1d} + D_{12d} D_{1k} C_{2d})^T$

The change in controller variables for the damping controller, namely A_{1k}, B_{1k}, C_{1k}, and D_{1k}, are computed using (5.10) and (5.11), respectively. Subsequently, the matrix coefficients for the damping controller A_k, B_k, C_k, and D_k, can be obtained from A_{1k}, B_{1k}, C_{1k}, and D_{1k} by using (5.9). The Robust Control Toolbox present in MATLAB is utilized to solve this LMI problem.

Another design objective is considered to ensure the robustness of the damping controller to place the poles of the prominent modes inside a conic sector to confirm the minimal damping ratio $\zeta_{min} = cos^{-1}\left(\frac{\theta}{2}\right)$ for all poles.

5.3.1 WADC design procedure for BESS

The self-explanatory flowchart depicted in Fig. 5.5 explains the H_∞ mixed sensitivity approach based WADC design procedure for the BESS integrated power network.

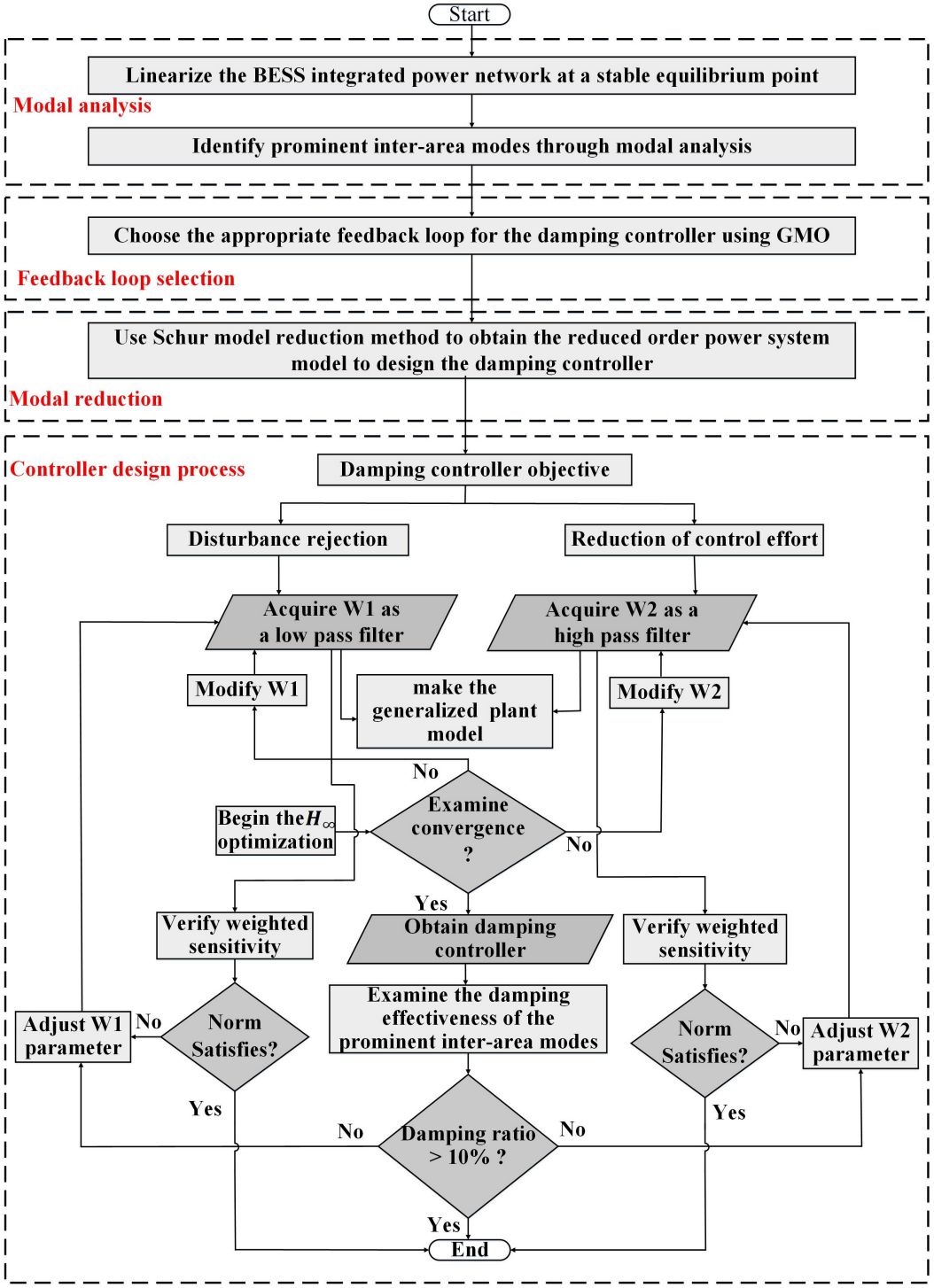

Figure 5.5: Flowchart to design WADC for BESS.

5.4 Verification of the WADC Performance on the Modified New England Ten-Machine System

5.4.1 Description of the study power system

The proposed H_∞ mixed sensitivity scheme based WADC for BESS is verified on the modified New England ten-machine benchmark power system, depicted in Fig. 5.6. The details of the study system are given in Appendix-C. The transmission lines connecting bus-3 and bus-2 (Area-1 to Area-3), bus-3 and bus-18 (Area-1 to Area-2), and bus-17 and bus-27 (Area-2 to Area-3) are the inter-area transmission lines in this practical study system that divide the entire system into three areas. The SG1-SG3, SG4-SG7, and SG8-SG10 are placed in Area-1, Area-2, and Area-3, respectively. The parameters of the study system are taken from [92]. The excitation systems of SG2, SG6, SG9, and SG10 were employed with PSS with gain taken as 50 times the PSS gain considered in [92]. PSS placement is based on participation factor analysis, which is presented in sub-section 5.4.4. The three BESS namely, BS1, BS2, and BS3 are integrated on bus-8 (Area-1), bus-29 (Area-3), and bus-20 (Area-2), respectively. The power capacity of each BESS is 50 MW. The VSC is modeled in this work as an aggregate model that is equivalent to the BESS capacity. One BESS was placed in each area to study their impact on inter-area oscillation.

The practical study test systems without and with BESS are referred as CS1 and CS2, respectively, in this work. Three operating conditions corresponding to 15% load increase in Area-1, Area-2 and Area-3, respectively, are represented as OC1, OC2, and OC3, respectively, as shown in Table 5.1.

5.4.2 Modal analysis

The modal analysis of the modified New England ten-machine benchmark power system is carried out in CS1 and CS2 under operating conditions OC1, OC2, and OC3 by using MATLAB/Simulink software. Table 5.2 shows this study system's eigenvalue and damping ratio for CS1. Under multiple operating conditions (i.e. OC1, OC2, OC3), this study system contains six inter-area modes (M1 to M6). It is observed from Table 5.2 that modes M2, M4, and M6 are prominent inter-area oscillation modes because their

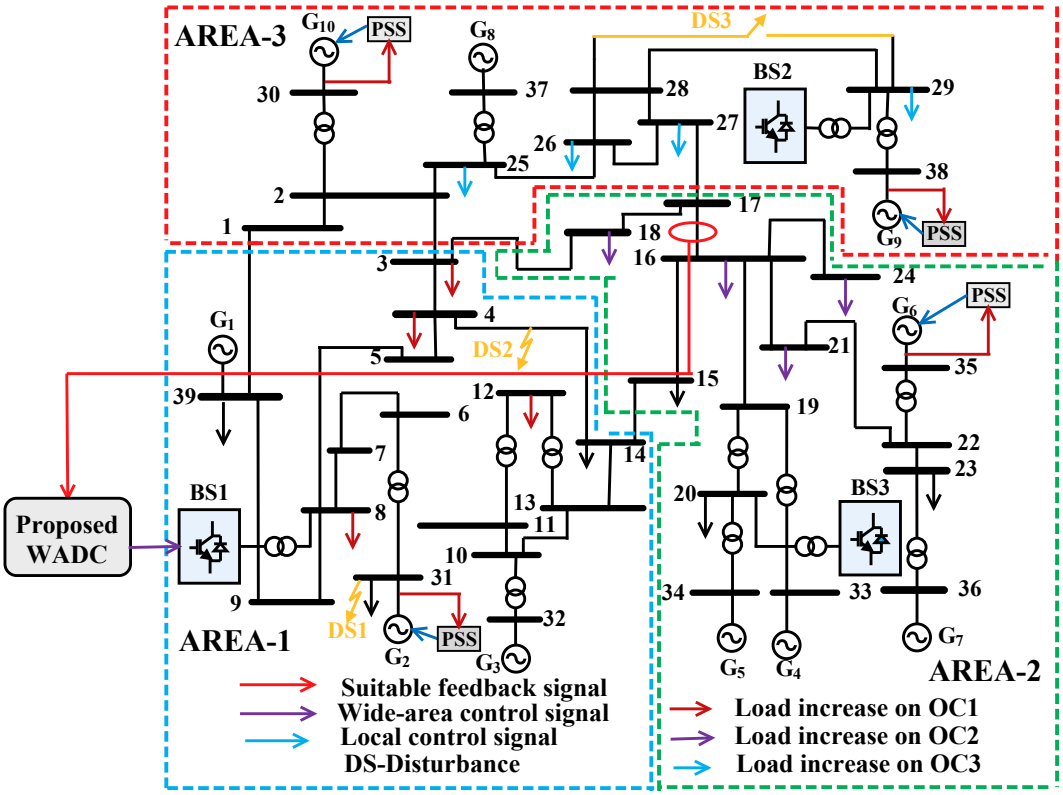

Figure 5.6: A modified New England ten-machine system.

Table 5.1: Operating conditions for the New England ten-machine benchmark system

Operating conditions	**Description of the system operating conditions**
OC1	The active and reactive power of loads in Area-1 (buses 3,4,8, &12) are increased to 15% of the rated value
OC2	The active and reactive power of loads in Area-2 (buses 16,18,21 &24) are increased to 15% of the rated value
OC3	The active and reactive power of loads in Area-3 (buses 25,26,27 &29) are increased to 15% of the rated value

damping ratios are less than 5%.

The damping performance of the system inter-area oscillation modes in CS1 and CS2 are listed in Table 5.3. The damping ratios of prominent inter-area modes M2, M4, and M6 are obtained as 3.37%, 4.84% and 3.93%, respectively in CS1, that increase to

Table 5.2: Eigenvalue of the study system operating under multiple conditions in CS1

Operating conditions	**Mode**	**Eigenvalue and damping ratio**	**Mode shape**
OC1	M1	$-0.330 \pm i5.162$ ($\xi = 6.37\%, f = 0.821$ Hz)	G_5, G_6, G_7 vs. G_8, G_{10} (Area-2 vs. Area-3
	M2	$\mathbf{-0.133 \pm i3.969}$ ($\boldsymbol{\xi = 3.37\%, f = 0.631}$ **Hz**)	$\boldsymbol{G_2, G_3}$ **vs.** $\boldsymbol{G_9, G_{10}}$ **(Area-1 vs. Area-3)**
OC2	M3	$-0.341 \pm i5.146$ ($\xi = 6.61\%, f = 0.819$ Hz)	G_4, G_5, G_7 vs. G_9, G_{10} (Area-2 vs. Area-3
	M4	$\mathbf{-0.189 \pm i3.898}$ ($\boldsymbol{\xi = 4.84\%, f = 0.620}$ **Hz**)	$\boldsymbol{G_5, G_6, G_7}$ **vs.** $\boldsymbol{G_9, G_{10}}$**,&**$\boldsymbol{G_2}$ **(Area-2 vs. Area-3 & Area-1)**
OC3	M5	$-0.322 \pm i5.158$ ($\xi = 6.23\%, f = 0.820$ Hz)	G_5, G_6 vs. G_8, G_9, G_{10} (Area-2 vs. Area-3
	M6	$\mathbf{-0.215 \pm i3.878}$ ($\boldsymbol{\xi = 3.93\%, f = 0.637}$ **Hz**)	$\boldsymbol{G_5, G_6, G_7}$ **vs.** $\boldsymbol{G_9, G_{10}}$ **(Area-2 vs. Area-3)**

Table 5.3: Eigenvalue of the study system under multiple operating conditions in CS1 and CS2

Operating conditions	**Mode**	**Damping ratio in CS1**	**Damping ratio in CS2**
OC1	M1	$-0.330 \pm i5.162$ ($\xi = 6.37\%, f = 0.821$ Hz)	$-0.347 \pm i5.098$ ($\xi = 6.805\%, f = 0.811$ Hz)
	M2	$\mathbf{-0.133 \pm i3.969}$ ($\boldsymbol{\xi = 3.37\%, f = 0.631}$ **Hz**)	$\mathbf{-0.175 \pm i3.938}$ ($\boldsymbol{\xi = 4.461\%, f = 0.626}$ **Hz**)
OC2	M3	$-0.341 \pm i5.146$ ($\xi = 6.61\%, f = 0.819$ Hz)	$-0.362 \pm i5.172$ ($\xi = 6.98\%, f = 0.823$ Hz)
	M4	$\mathbf{-0.189 \pm i3.898}$ ($\boldsymbol{\xi = 4.84\%, f = 0.620}$ **Hz**)	$\mathbf{-0.215 \pm i3.916}$ ($\boldsymbol{\xi = 5.49\%, f = 0.623}$ **Hz**)
OC3	M5	$-0.322 \pm i5.158$ ($\xi = 6.23\%, f = 0.820$ Hz)	$-0.356 \pm i5.167$ ($\xi = 6.88\%, f = 0.822$ Hz)
	M6	$\mathbf{-0.215 \pm i3.878}$ ($\boldsymbol{\xi = 3.93\%, f = 0.637}$ **Hz**)	$\mathbf{-0.189 \pm i3.973}$ ($\boldsymbol{\xi = 4.75\%, f = 0.632}$ **Hz**)

4.46% ,5.49% and 4.75%, respectively in CS2. Moreover, other modes' damping ratio are marginally increased in CS2 compared to CS1. This shows that BESS integration to the system improves damping of prominent inter-area modes of oscillation.

5.4.3 Eigenvalue of study system under different operating conditions using Monte Carlo simulation

A Monte Carlo-based probabilistic stability analysis using normal distributions is conducted with 20,000 iterations to examine the impact of load variation on damping of prominent oscillation modes. The Monte Carlo simulation is suggested in [96] to analyze the damping performance of the system for low-frequency oscillation. Loads were varied at buses 3, 4, 8, and 12 in Area-1. The mean and standard deviation of Area-1's load variation, assuming the standard deviation as 10% of the mean load variation, are shown in Table 5.4. The histogram plot of load variations are shown in Fig. 5.7. Assessing the damping performance of the predominant inter-area mode M2 under operating condition OC1, the analysis considers different candidate groups (L1 to L7) of load variation obtained from the histogram plot, with the result shown in Table 5.4.

Table 5.4: Analysis of load variation and damping performance of study system under operating condition OC1

Load variation at different buses		**Bus 3**		**Bus4**		**Bus 8**		**Bus 12**		**Eigenvalue & damping ratio**	
		P (MW)	**Q (MVAR)**	**P (MW)**	**Q (MVAR)**	**P (MW)**	**Q (MVAR)**	**P (MW)**	**Q (MVAR)**		
Mean of load variation		48	0.36	75	27.6	78	26.4	1.27	13.2		
Standard deviation of load variation		4.8	0.036	7.5	2.7	7.8	2.64	0.127	1.32	**Mode M1**	**Mode M2**
Candidate group of load variation	**L1**	362.7	2.684	560	206.3	584.8	197.6	9.518	98.05	$-0.359 \pm i5.443$ ($\xi = 6.59\%, f = 0.866$ Hz)	$\mathbf{-0.169 \pm i3.824}$ ($\boldsymbol{\xi = 4.41\%, f = 0.608}$ **Hz**)
	L2	364.4	2.712	565.4	208.5	589.7	199.5	9.632	99.34	$-0.346 \pm i5.388$ ($\xi = 6.41\%, f = 0.857$ Hz)	$\mathbf{-0.142 \pm i3.872}$ ($\boldsymbol{\xi = 3.665\%, f = 0.616}$ **Hz**)
	L3	366	2.733	570.8	210.2	593.4	201.6	9.736	100.3	$-0.48 \pm i5.392$ ($\xi = 6.44\%, f = 0.858$ Hz)	$\mathbf{-0.133 \pm i3.924}$ ($\boldsymbol{\xi = 3.41\%, f = 0.624}$ **Hz**)
	L4	370	2.76	575	211.6	600	203.09	9.81	101.21	$-0.330 \pm i5.162$ ($\xi = 6.37\%, f = 0.821$ Hz)	$\mathbf{-0.133 \pm i3.969}$ ($\boldsymbol{\xi = 3.37\%, f = 0.631}$ **Hz**)
	L5	372.8	2.78	579.8	212.8	606.4	204.5	9.872	102.1	$-0.325 \pm i5.117$ ($\xi = 6.356\%, f = 0.81$ Hz)	$\mathbf{-0.129 \pm i3.921}$ ($\boldsymbol{\xi = 3.28\%, f = 0.624}$ **Hz**)
	L6	374.9	2.798	583.4	214.8	610.1	206.4	9.965	103	$-0.308 \pm i5.025$ ($\xi = 6.13\%, f = 0.799$ Hz)	$\mathbf{-0.105 \pm i3.581}$ ($\boldsymbol{\xi = 2.93\%, f = 0.569}$ **Hz**)
	L7	377	2.832	589.4	217.1	615.6	208.9	10.1	104.3	$-0.323 \pm i5.121$ ($\xi = 6.30\%, f = 0.815$ Hz)	$\mathbf{-0.127 \pm i3.829}$ ($\boldsymbol{\xi = 3.31\%, f = 0.609}$ **Hz**)

The eigenvalue analysis results shown in Table 5.4 reveal that the damping ratio of the predominant inter-area mode M2 gets decreased compared to 15% of load variation candidate group L4 (i.e., the same load variation as shown in Table 5.1) if the load variation in Area-1 is above 15% (load variation groups L5 to L7). Further, the damping performance of predominant mode M2 gets increased in the candidate group of load variation L1 to L3 compared to 15% of load variation candidate group L4 as these groups have less than 15% load increase.

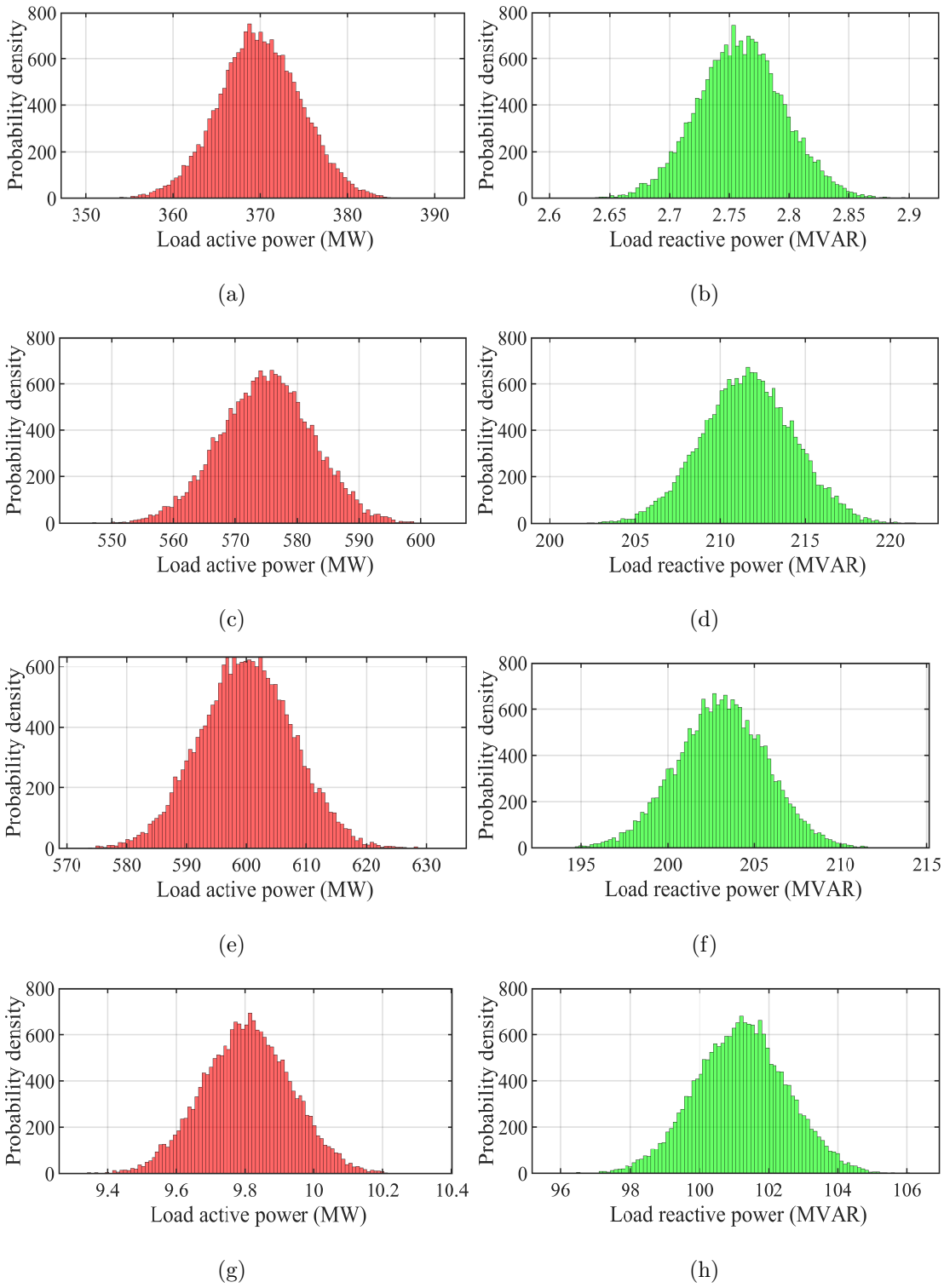

Figure 5.7: Histogram plot of load variation of study system under operating condition OC1. (a) Bus-3 active power, (b) Bus-3 reactive power, (c) Bus-4 active power, (d) Bus-4 reactive power,(e) Bus-8 active power, (f) Bus-8 reactive power,(g) Bus-12 active power, and (h) Bus-12 reactive power.

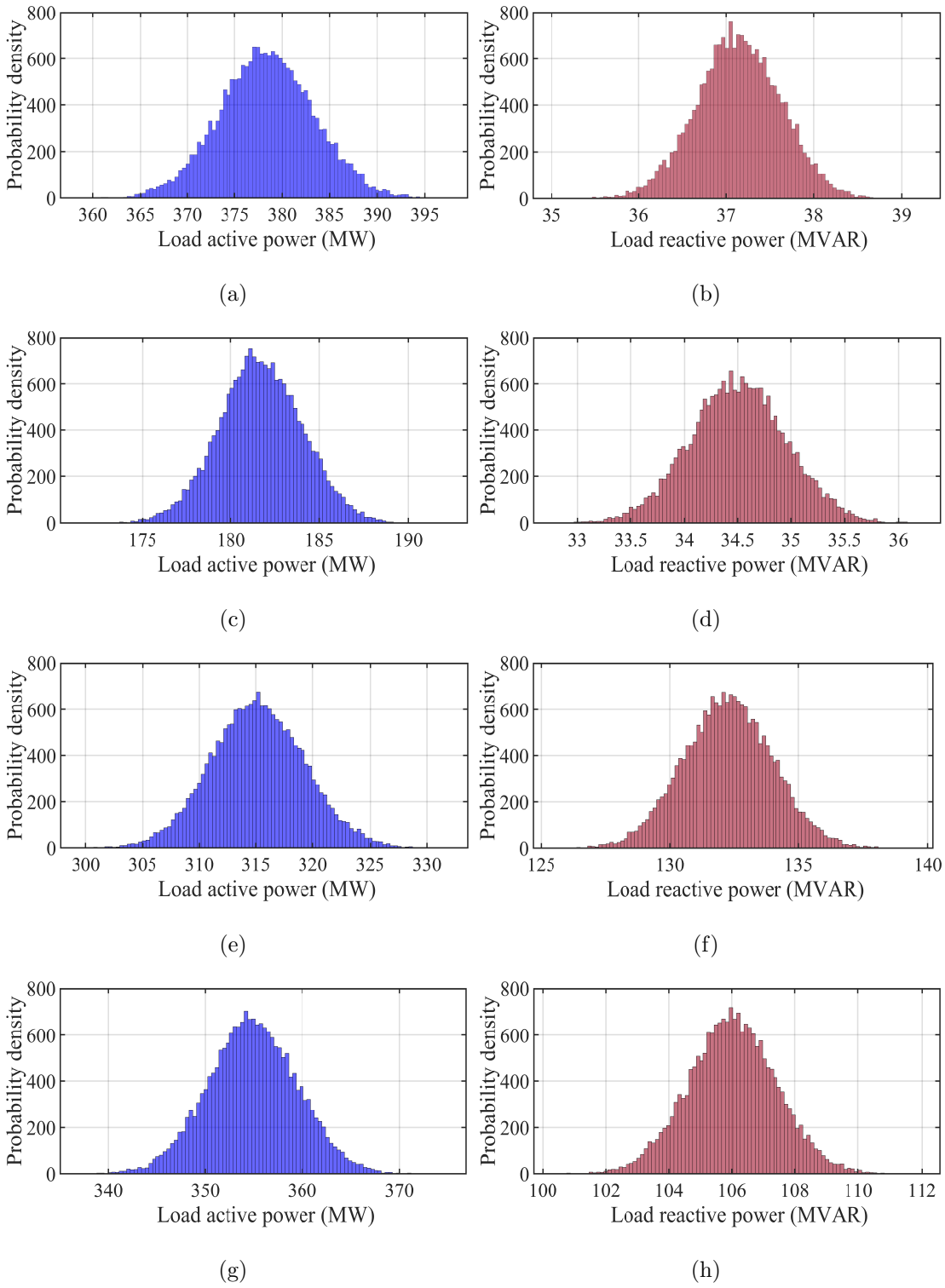

Figure 5.8: Histogram plot of load variation of study system under operating condition OC2. (a) Bus-16 active power, (b) Bus-16 reactive power, (c) Bus-18 active power, (d) Bus-18 reactive power,(e) Bus-21 active power, (f) Bus-21 reactive power,(g) Bus-24 active power, and (h) Bus-24 reactive power.

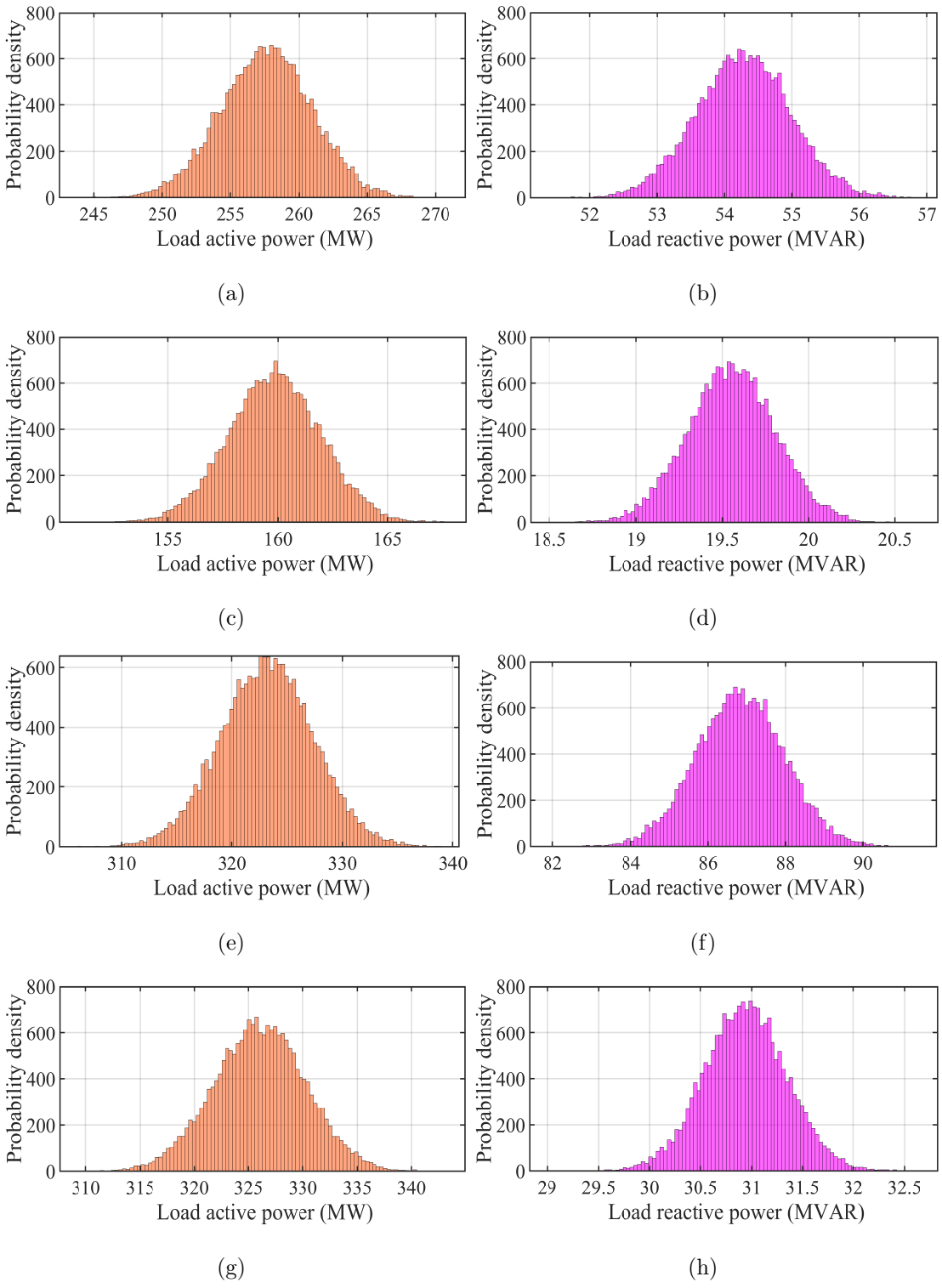

Figure 5.9: Histogram plot of load variation of study system under operating condition OC3. (a) Bus-25 active power, (b) Bus-25 reactive power, (c) Bus-26 active power, (d) Bus-26 reactive power,(e) Bus-27 active power, (f) Bus-27 reactive power,(g) Bus-29 active power, and (h) Bus-29 reactive power.

Table 5.5: Analysis of load variation and damping performance of study system under operating condition OC2

Load variation at different buses		**Bus 16**		**Bus 18**		**Bus 21**		**Bus 24**		**Eigenvalue & damping ratio**	
		P (MW)	**Q (MVAR)**	**P (MW)**	**Q (MVAR)**	**P (MW)**	**Q (MVAR)**	**P (MW)**	**Q (MVAR)**		
Mean of load variation		49.35	4.845	23.7	4.5	41.1	17.25	46.29	13.83		
Standard deviation of load variation		4.935	0.484	2.37	0.45	4.11	1.725	4.62	1.383	**Mode M3**	**Mode M4**
Candidate group of load variation	**L1**	367.5	35.85	176.8	33.42	307.6	128.9	345.3	102.9	$-0.337 \pm i5.189$ ($\xi = 6.49\%, f = 0.825$ Hz)	$\mathbf{-0.203 \pm i3.978}$ ($\boldsymbol{\xi = 5.09\%, f = 0.634}$ **Hz**)
	L2	371.8	36.44	178.9	33.87	310.5	130.2	349.1	104.2	$-0.339 \pm i5.104$ ($\xi = 6.64\%, f = 0.812$ Hz)	$\mathbf{-0.200 \pm i4.013}$ ($\boldsymbol{\xi = 4.99\%, f = 0.638}$ **Hz**)
	L3	374.5	36.78	180.6	34.18	313.1	131.3	352.1	105.2	$-0.338 \pm i5.162$ ($\xi = 6.54\%, f = 0.821$ Hz)	$\mathbf{-0.198 \pm i4.059}$ ($\boldsymbol{\xi = 4.87\%, f = 0.646}$ **Hz**)
	L4	378.37	37.14	181.68	34.5	315.1	132.26	354.89	106.02	$-0.341 \pm i5.146$ ($\xi = 6.61\%, f = 0.819$ Hz)	$\mathbf{-0.189 \pm i3.898}$ ($\boldsymbol{\xi = 4.84\%, f = 0.620}$ **Hz**)
	L5	381.2	37.45	182.9	34.84	316.4	133.6	357.1	106.9	$-0.320 \pm i5.175$ ($\xi = 6.18\%, f = 0.823$ Hz)	$\mathbf{-0.169 \pm i3.803}$ ($\boldsymbol{\xi = 4.45\%, f = 0.605}$ **Hz**)
	L6	384.7	37.92	184.4	35.08	319.6	134.6	360.5	107.7	$-0.346 \pm i5.452$ ($\xi = 6.35\%, f = 0.867$ Hz)	$\mathbf{-0.172 \pm i4.028}$ ($\boldsymbol{\xi = 4.28\%, f = 0.641}$ **Hz**)
	L7	388.6	38.3	187.3	35.56	322.5	136.4	364.3	109	$-0.294 \pm i5.041$ ($\xi = 5.838\%, f = 0.802$ Hz)	$\mathbf{-0.182 \pm i3.942}$ ($\boldsymbol{\xi = 4.62\%, f = 0.627}$ **Hz**)

Table 5.6: Analysis of load variation and damping performance of study system under operating condition OC3

Load variation at different buses		**Bus 25**		**Bus 26**		**Bus 27**		**Bus 29**		**Eigenvalue & damping ratio**	
		P (MW)	**Q (MVAR)**	**P (MW)**	**Q (MVAR)**	**P (MW)**	**Q (MVAR)**	**P (MW)**	**Q (MVAR)**		
Mean of load variation		33.6	7.08	20.85	2.55	42.15	11.32	42.52	4.03		
Standard deviation of load variation		3.36	0.708	2.08	0.25	4.21	1.13	4.25	0.40	**Mode M5**	**Mode M6**
Candidate group of load variation	**L1**	250	52.38	155.1	18.82	314.9	83.89	316.8	29.92	$-0.338 \pm i5.184$ ($\xi = 6.51\%, f = 0.825$ Hz)	$\mathbf{-0.181 \pm i3.821}$ ($\boldsymbol{\xi = 4.73\%, f = 0.608}$ **Hz**)
	L2	253.3	53.26	157.1	19.14	318.2	85.32	320.83	30.39	$-0.355 \pm i5.428$ ($\xi = 6.53\%, f = 0.863$ Hz)	$\mathbf{-0.168 \pm i3.782}$ ($\boldsymbol{\xi = 4.437\%, f = 0.601}$ **Hz**)
	L3	256.5	53.92	158.5	19.4	321.1	86.36	324.6	30.72	$-0.330 \pm i5.184$ ($\xi = 6.36\%, f = 0.825$ Hz)	$\mathbf{-0.172 \pm i4.028}$ ($\boldsymbol{\xi = 4.28\%, f = 0.641}$ **Hz**)
	L4	257.68	54.28	159.85	19.55	323.17	86.82	326.02	30.94	$-0.322 \pm i5.158$ ($\xi = 6.23\%, f = 0.820$ Hz)	$\mathbf{-0.215 \pm i3.878}$ ($\boldsymbol{\xi = 3.93\%, f = 0.637}$ **Hz**)
	L5	259.2	54.79	161	19.68	325.4	87.5	327.9	31.15	$-0.294 \pm i5.041$ ($\xi = 5.83\%, f = 0.802$ Hz)	$\mathbf{-0.147 \pm i3.861}$ ($\boldsymbol{\xi = 3.80\%, f = 0.614}$ **Hz**)
	L6	261.4	55.34	162.7	19.91	328.4	88.26	331	31.41	$-0.308 \pm i5.035$ ($\xi = 6.11\%, f = 0.801$ Hz)	$\mathbf{-0.139 \pm i4.06}$ ($\boldsymbol{\xi = 3.42\%, f = 0.646}$ **Hz**)
	L7	265.7	56.05	164.5	20.25	331.7	89.78	336.1	31.95	$-0.319 \pm i5.182$ ($\xi = 6.15\%, f = 0.824$ Hz)	$\mathbf{-0.130 \pm i3.85}$ ($\boldsymbol{\xi = 3.37\%, f = 0.612}$ **Hz**)

Further, the histogram plot of load variation of the study system under operating conditions OC2 and OC3 are obtained using the Monte Carlo simulation with load variations at buses 16, 18, 21, and 24 in Area-2 and at buses 25, 26, 27, and 29 in Area-3. The histogram plots are shown in Fig. 5.8 and Fig. 5.9, respectively, for Area-2 and Area-3, respectively. The mean and standard deviation of load variation, along with the damping performance of the system under OC2 and OC3, are shown in Table 5.5 and Table 5.6. It is observed from Table 5.5 that load variation in Area-2 above 15% results in deterioration

in damping of prominent mode M4, whereas load variation below 15% increase has higher damping compared to 15% load increase. It is observed from Table 5.6 that load increases beyond 15% causes decrease in damping of prominent mode M6, whereas load variations below 15% load increase has higher damping compared to 15% load increase.

This analysis reveals a change in the damping performance of the system's prominent inter-area modes under variations in load, as assessed through the Monte Carlo simulation-based probabilistic method. Therefore, proposed WADC design has given due consideration to the impact of load variations on low-frequency oscillations.

5.4.4 Location of PSS in inter-area modes

The location of PSS in the prominent oscillation modes of the practical study system operating under case CS1 is obtained using the participation factor method [82]. The participation factor plot of rotor speed corresponding to prominent inter-area oscillation modes is shown in Fig. 5.10 for the ten synchronous generators present in the system. It is observed from Fig. 5.10 that rotor speed of SG6 and SG9 corresponding to mode M2 , SG2 and SG10 corresponding to mode M4 and SG9 and SG10 corresponding to mode M6 have highest participation factor. Therefore, PSS were placed in the excitation system of SG2, SG6, SG9 and SG10, as shown in Fig. 5.6.

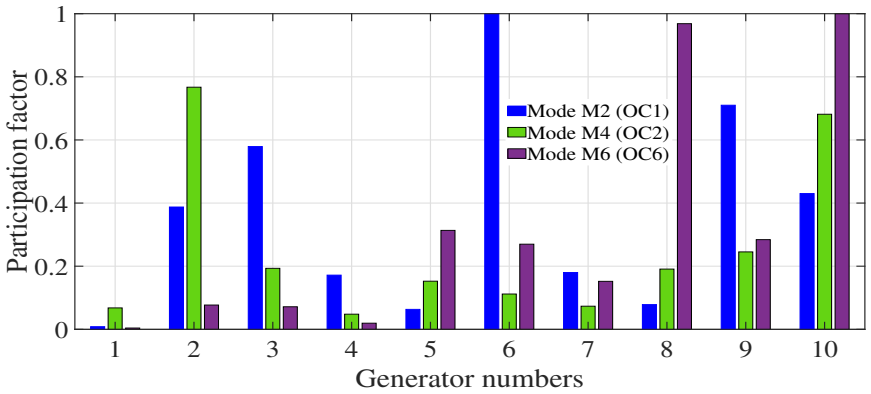

Figure 5.10: Participation factor plot of the study system in prominent inter-area oscillation modes.

5.4.5 Impact of BESS on power system inter-area modes

5.4.5.1 BESS control mode dynamic interaction

The participation factor analysis evaluates each state variable influencing the system's prominent oscillation mode [82]. Fig. 5.11 illustrates the contribution of the dynamic state of the study system with the integration of multiple BESS to prominent inter-area oscillation modes. As per Fig. 5.11, the electro-mechanical states of SG (ω, and δ), and BESS states, i.e., PLL states (x_{pll}, and θ_{pll}), battery pack states (V_1, V_2, and I_b), dc-link voltage state (V_{dc}), VSC current states (I_{cd}, and I_{cq}, power control loop states (x_{p1}, and x_{q1}), and current control loop states (x_{p2}, and x_{q2}), are the primary causes to affect the system's prominent inter-area modes under various operating conditions. It is observed that close loop control mode dynamic interaction between SG and BESS affects the system's prominent inter-area modes.

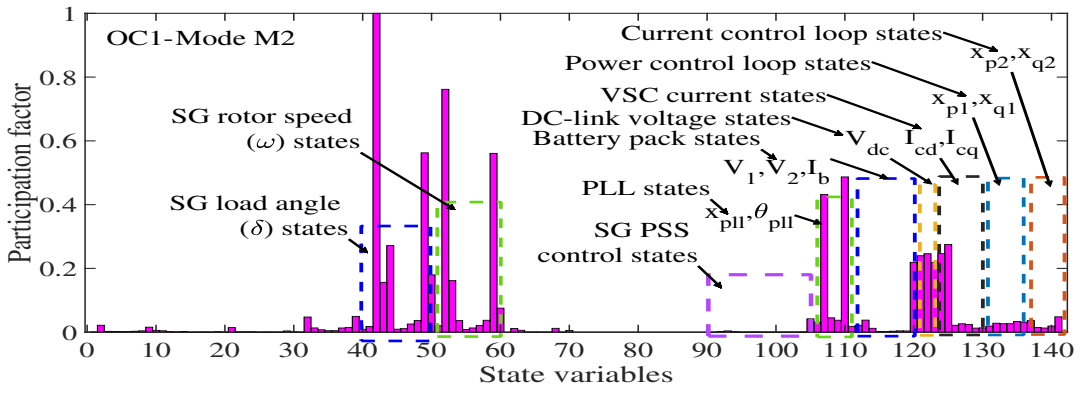

(a)

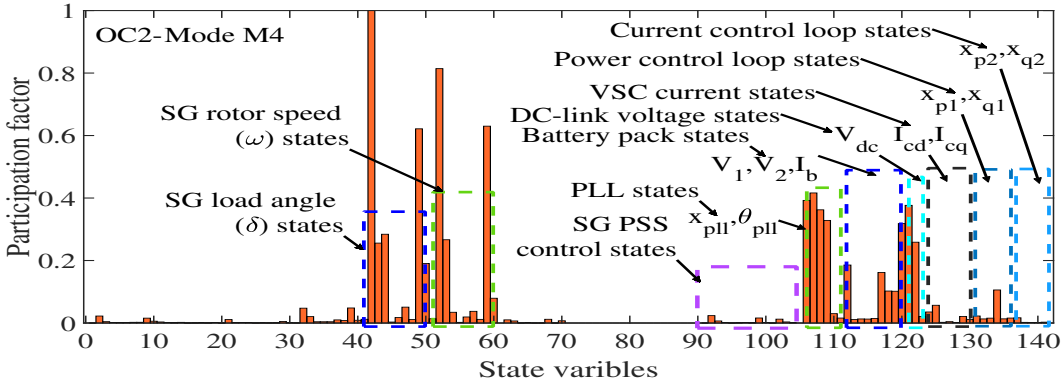

(b)

Figure 5.11: Contribution of BESS control mode in prominent inter-area modes M2 and M4.(a) System operating on OC1 and (b) System operating on OC2.

Moreover, the influence of the states $I_{cd}, I_{cq}, x_{p1}, x_{q1}, x_{p2}$, and x_{q2} in the study system's inter-area mode M2 operating on OC1 is significantly greater than that of operating condition OC2. However, when the study system is operated under operating condition OC2, the contribution of the states $x_{pll}, \theta_{pll}, V_{dc}, V_1, V_2$, and I_b in inter-area mode M4 is much more than that of operating condition OC1. As a result, depending on the changing loading conditions, the BESS control mode affects the power system's inter-area modes. As a result, in addition to the interaction between SG and BESS in close loop control mode, the change in system operating conditions also affects the power system's inter-area modes.

5.4.5.2 Identification of sensitive BESS control parameters on inter-area modes

The BESS control parameter's sensitivity to prominent inter-area modes is depicted in Fig. 5.12. The parametric sensitivity method is described in [97]. The prominent inter-area mode moves from the left-half plane to the right-half plane with an increase in the related control parameter when the sensitivity is positive and vice versa. The magnitude of sensitivity designates the prominent inter-area mode's movement velocity as it responds to parameter variation.

In Fig. 5.12, K_{ppll} and K_{ipll} are the PI controller gain coefficient of PLL, respectively; K_{pp}, K_{ip}, K_{pq}, and K_{iq} are the PI controller gain coefficients of active and reactive power control loops, respectively; $K_{pi_{cd}}, K_{ii_{cd}}, K_{pi_{cq}}$, and $K_{ii_{cq}}$ are the PI controller gain coefficients of the d and q-axis current control loops, respectively as shown in Fig. 4.2 of chapter-4.

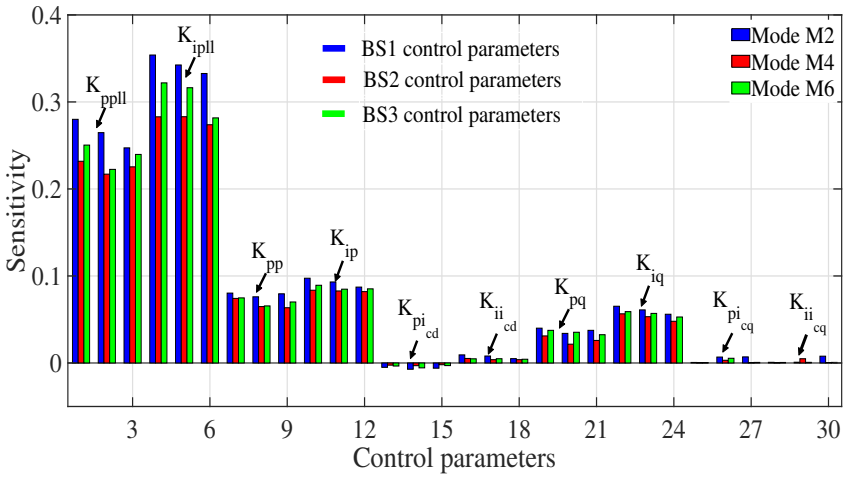

Figure 5.12: BESS control parameters sensitivity to prominent inter-area modes.

The PI controller gain of PLL and the PI controller gain of the active and reactive power control loop have high sensitivity to prominent inter-area modes under operating condition OC1 as compared to OC2 and OC3, as depicted in Fig. 5.12. Therefore the damping of prominent inter-area modes is diminished with the increase of K_{pp}, K_{ip}, K_{pq}, and K_{iq} gain of the PI controller. The active current proportional loop gain $K_{pi_{cd}}$ has lower sensitivity (negative sensitivity) to prominent inter-area modes, demonstrating that an increase in $K_{pi_{cd}}$ can enhance oscillation mode damping. Thus, the sensitivity to BESS control mode parameters affects the power system inter-area modes damping under the change in operating conditions.

5.4.6 Design of WADC for BESS

5.4.6.1 Control loop selection for the WADC

The GMO approach, which is explained in Section 5.2.2.1 is used to choose the proper feedback signal for the WADC. The GMO of the practical study system of the active power flow through all the transmission lines for prominent inter-area modes M2, M4, and M6 are shown in Fig. 5.13. As can be seen, the power flow through line 26 (that corresponds to line 16–17) has maximum observability (0.1837) for mode M2 that is highest value of GMO among all the lines for the three dominant modes considered. Therefore, the active power flows in this line 16–17 is chosen as the appropriate feedback signal for the WADC.

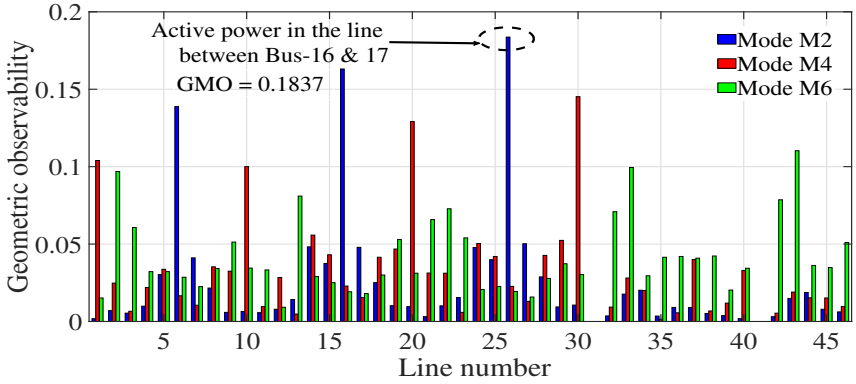

Figure 5.13: GMO of line active power.

The active power control loop of the BESS is more sensitive to the BESS control mode parameter than the reactive power control loop for the prominent inter-area modes, as depicted in Fig. 5.12. In comparison to other BESSs (i.e., BS2 and BS3), it was found that the BS1 active power control loop was highly sensitive to the BESS control

mode parameter corresponding to prominent inter-area mode M2. Therefore, WADC was installed at BS1, as shown in Fig. 5.6.

5.4.6.2 Design of H_∞ mixed sensitivity scheme-based WADC

The WADC for the BS1, integrated into the study test system, is depicted in Fig. 5.6. The multiobjective H_∞ mixed sensitivity control design scheme is discussed in Section 5.3. The full order of the open-loop plant model of the study system is obtained as 158^{th}-order using P_{16-17} as the output and u_p as the input of BS1. It also includes a 200 ms communication delay in the output signal. The complexity of the WADC design is decreased by reducing this higher-order system to the 10^{th}-order system by using the Schur model reduction approach [44]. The frequency response of the full-order and reduced-order systems are depicted in Fig. 5.14(a). As can be seen, in the frequency range (0.1–2 Hz), the reduced-order system's frequency response is approximately similar to that of the full-order system. The reduced order system includes the prominent inter-area oscillation mode M2.

The procedure for designing the BESS-based WADC is described in Subsection 5.3.1. The generalized plant with the appropriate weight shaping filter is selected by using MATLAB function *sysic*. The positioning of the prominent inter-area mode M2 poles is within the conic sector, and the 10% of minimum damping ratio is essential for designing the controller. As a result, the inner angle $\theta = 2cos^{-1}(0.1) = 168.521^\circ$ corresponds to this damping ratio. The LMI region is defined using the MATLAB function *lmireg*.

The H_∞ mixed sensitivity control scheme is solved in the LMI framework using the *hinfmix* function in MATLAB. The W1(s) and W2(s) designed in the H_∞ performance channel are selected to intersect at about 10 rad/s since all prominent inter-area modes are below this frequency. The weight functions are chosen to design the WADC for BS1 as follows:

$$W1(s) = 0.675\left(\frac{50}{s+50}\right), W2(s) = 0.675\left(\frac{50s}{s+50}\right) \tag{5.12}$$

The order of the designed WADC for BS1 is relatively high (the weighting function order plus reduced order open loop plant order, i.e., 12^{th} order), which may be unfeasible from application perspective. Thus, the Schur model reduction technique is carried out to reduce the order of the designed WADC to the 6^{th} order. The full-order and reduced-order WADC's frequency responses are depicted in Fig. 5.14(b). As can be observed, the

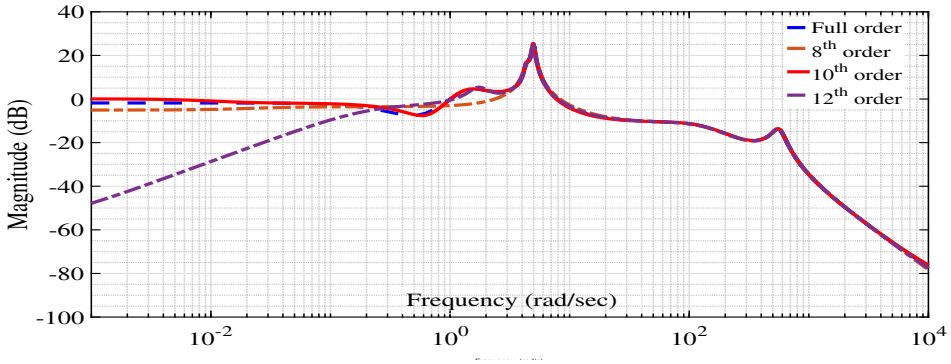

(a)

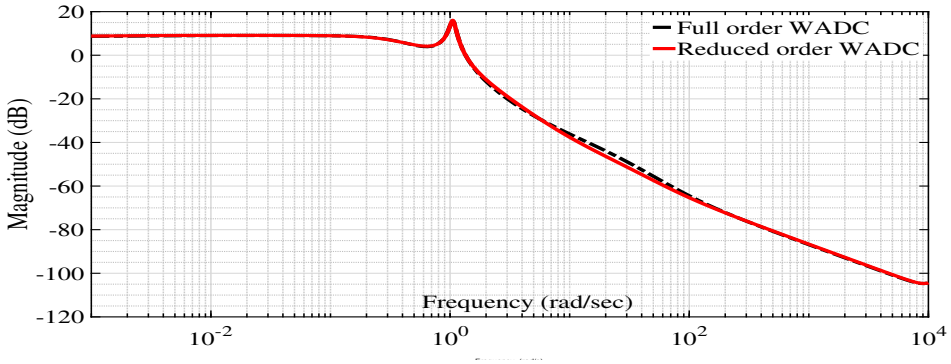

(b)

Figure 5.14: Frequency response plot. (a) The modified New England ten-machine system with BESS, (b) Designed WADC for BS1.

reduced-order and full-order designed WADC have comparable frequency characteristics. The reduced-order WADC model for BS1 is obtained as follows:

$$G_{kr}(s) = \frac{N_{kr}(s)}{D_{kr}(s)} \tag{5.13}$$

where $N_{kr}(s) = 0.1383s^5 + 44.24s^4 + 1.79\times10^7 s^3 + 3.78\times10^8 s^2 - 2.38\times10^9 s + 4.34\times10^9$

$$D_{kr}(s) = s^6 - 362s^5 + 1.33\times10^8 s^4 - 1.86\times10^9 s^3 + 4.50\times10^9 s^2 - 1.26\times10^9 s + 4.88\times10^9$$

5.4.7 Performance verification of H_∞ mixed sensitivity scheme based WADC

The damping performance of the proposed H_∞ mixed sensitivity scheme-based WADC for the BS1 is assessed using modal analysis under the various operating conditions of the study test system. The proposed WADC's damping ratio in inter-area modes with

the power system operating without fault condition is shown in Table 5.7. It has been found that the proposed WADC increases the damping ratio of the inter-area modes M1 to M6 by more than 10%. Furthermore, this work compares the proposed WADC with the already used ESS-based stabilizer design approach suggested in [66] and the WADC design scheme presented in [61]. In the ESS-based stabilizer [66] and WADC [61] designs, the P_{sref} is taken into account as the input, and P_{16-17} is the feedback signal with a 200 ms communication time delay. It is observed from Table 5.7 that the damping ratio for each inter-area oscillation mode (i.e., M1 to M6) is less than 10% for ESS-based stabilizer presented in [66]. On the other hand, the damping ratio of WADC [61] in inter-area modes M1 and M2 are lower than 10%, while the other inter-area oscillation Modes M3 to M6 are slightly higher than 10%. So, damping performance of WADC [61] is better than the ESS-based stabilizer [66]. It is observed from Table 5.7 that proposed H_∞ mixed sensitivity scheme-based WADC gives more than 10% damping under all three operating conditions (OC1, OC2, and OC3). Apart from this, proposed WADC gives better damping compared to ESS-based stabilizer [66] and WADC suggested in [61] for all six modes (M1 to M6) under all three operating conditions (OC1, OC2, and OC3) considered in this work. Under various operating conditions, ESS-based stabilizer [66] and WADC [61] are less capable of providing sufficient damping to prominent inter-area oscillation modes. Proposed WADC provides superior damping performance for the system's prominent inter-area modes compared to the ESS-based stabilizer [66] and WADC [61] under changing operating scenarios.

Furthermore, to confirm the robustness of the proposed WADC, this work introduces 200 ms and 300 ms communication time delays in the feedback signal using the satellite communication network. The damping performance of the proposed WADC as well as two existing controllers (viz. ESS-based stabilizer [66] and WADC proposed in [61]) under 200 ms and 300 ms communication time delays are shown in Table 5.8. It is observed from Table 5.8 that proposed WADC is more effective in damping prominent modes of inter-area oscillation compared to two existing controllers even under different communication time delays.

From the result shown in Table 5.7 and 5.8, we can say that the proposed WADC provides robust damping performance for prominent inter-area modes against the uncertainty of the change in system operating conditions and feedback signal communication

Table 5.7: Damping performance of the study system with WADCs for inter-area modes in CS2

Operating conditions	**Mode**	**ESS-based stabilizer [66]**	**WADC [61]**	**Proposed WADC**
OC1	M1	$-0.418 \pm i4.983$ ($\xi = 8.35\%$)	$-0.379 \pm i4.017$ ($\xi = 9.39\%$)	$-0.439 \pm i3.685$ ($\xi = 11.84\%$)
	M2	$\mathbf{-0.318 \pm i4.563}$ ($\boldsymbol{\xi = 6.95\%}$)	$\mathbf{-0.404 \pm i4.102}$ ($\boldsymbol{\xi = 9.86\%}$)	$\mathbf{-0.473 \pm i3.836}$ ($\boldsymbol{\xi = 12.24\%}$)
OC2	M3	$-0.371 \pm i3.75$ ($\xi = 9.85\%$)	$-0.429 \pm i4.024$ ($\xi = 10.59\%$)	$-0.643 \pm i4.876$ ($\xi = 13.07\%$)
	M4	$\mathbf{-0.359 \pm i4.563}$ ($\boldsymbol{\xi = 7.84\%}$)	$\mathbf{-0.368 \pm i3.594}$ ($\boldsymbol{\xi = 10.18\%}$)	$\mathbf{-0.469 \pm i3.869}$ ($\boldsymbol{\xi = 12.03\%}$)
OC3	M5	$-0.375 \pm i4.111$ ($\xi = 9.09\%$)	$-0.489 \pm i4.804$ ($\xi = 10.12\%$)	$-0.479 \pm i3.324$ ($\xi = 14.26\%$)
	M6	$\mathbf{-0.426 \pm i4.768}$ ($\boldsymbol{\xi = 8.90\%}$)	$\mathbf{-0.403 \pm i4.073}$ ($\boldsymbol{\xi = 10.01\%}$)	$\mathbf{-0.472 \pm i3.665}$ ($\boldsymbol{\xi = 12.77\%}$)

delays.

5.4.8 Eigenvalue analysis of the H_∞ mixed sensitivity scheme based WADC under various contingencies

The damping performance of the proposed WADC, ESS-based stabilizer [66], and WADC [61] under contingencies are shown in Table 5.9. In this study, a three-phase fault (at t = 3 sec for 0.1 sec) is applied to the terminal of SG2 of the study system operating under OC1. As demonstrated in Table 5.9, the damping performance of the proposed controller is significantly better for inter-area modes M1 and M2 than that of the ESS-based stabilizer [66] and the WADC [61].

To further establish the robustness of the proposed WADC, a three-phase fault (at t = 3 sec for 0.1 sec) is considered in line 4-14 under operating condition OC2. In contrast to ESS-based stabilizer [66] and WADC [61], the damping performance of the proposed controller significantly improves for inter-area oscillation modes M3 and M4, as shown in Table 5.9. In order to assess the damping effect of the proposed WADC under contingency for operating condition OC3, a three-phase fault (at t = 3 sec for 0.1 sec) is applied to the transmission line 27-17, supplemented with the outage of the line between buses 28 and

Table 5.8: Damping performance of the study system under different communication delays

Operating conditions	**Mode**	$T_d(ms)$	**ESS-based stabilizer [66]**	**WADC [61]**	**Proposed WADC**
OC1	M1	200	$-0.413 \pm i4.957$ ($\xi = 8.32\%$)	$-0.381 \pm i4.061$ ($\xi = 9.34\%$)	$-0.398 \pm i3.549$ ($\xi = 11.15\%$)
		300	$-0.399 \pm i4.834$ ($\xi = 8.22\%$)	$-0.457 \pm i4.928$ ($\xi = 9.27\%$)	$-0.353 \pm i3.460$ ($\xi = 10.15\%$)
	M2	200	$\mathbf{-0.307 \pm i4.594}$ ($\boldsymbol{\xi = 6.74\%}$)	$\mathbf{-0.402 \pm i4.100}$ ($\boldsymbol{\xi = 9.77\%}$)	$\mathbf{-0.392 \pm i3.513}$ ($\boldsymbol{\xi = 11.09\%}$)
		300	$\mathbf{-0.301 \pm i4.639}$ ($\boldsymbol{\xi = 6.48\%}$)	$\mathbf{-0.335 \pm i3.450}$ ($\boldsymbol{\xi = 9.66\%}$)	$\mathbf{-0.398 \pm i3.549}$ ($\boldsymbol{\xi = 11.15\%}$)
OC2	M3	200	$-0.466 \pm i4.920$ ($\xi = 9.43\%$)	$-0.484 \pm i4.638$ ($\xi = 10.43\%$)	$-0.472 \pm i3.665$ ($\xi = 12.77\%$)
		300	$-0.375 \pm i4.094$ ($\xi = 9.14\%$)	$-0.420 \pm i4.039$ ($\xi = 10.36\%$)	$-0.436 \pm i3.502$ ($\xi = 12.35\%$)
	M4	200	$\mathbf{-0.352 \pm i4.563}$ ($\boldsymbol{\xi = 7.69\%}$)	$\mathbf{-0.394 \pm i3.861}$ ($\boldsymbol{\xi = 10.15\%}$)	$\mathbf{-0.450 \pm i3.854}$ ($\boldsymbol{\xi = 11.6\%}$)
		300	$\mathbf{-0.335 \pm i4.45}$ ($\boldsymbol{\xi = 7.512\%}$)	$\mathbf{-0.388 \pm i3.859}$ ($\boldsymbol{\xi = 10.01\%}$)	$\mathbf{-0.443 \pm i3.993}$ ($\boldsymbol{\xi = 11.03\%}$)
OC3	M5	200	$-0.447 \pm i5.173$ ($\xi = 8.62\%$)	$-0.487 \pm i4.829$ ($\xi = 10.03\%$)	$-0.489 \pm i3.432$ ($\xi = 14.10\%$)
		300	$-0.409 \pm i4.857$ ($\xi = 8.39\%$)	$-0.403 \pm i4.037$ ($\xi = 9.94\%$)	$-0.562 \pm i4.291$ ($\xi = 12.98\%$)
	M6	200	$\mathbf{-0.451 \pm i5.202}$ ($\boldsymbol{\xi = 8.65\%}$)	$\mathbf{-0.495 \pm i4.898}$ ($\boldsymbol{\xi = 10.05\%}$)	$\mathbf{-0.579 \pm i4.464}$ ($\boldsymbol{\xi = 12.37\%}$)
		300	$\mathbf{-0.405 \pm i4.865}$ ($\boldsymbol{\xi = 8.31\%}$)	$\mathbf{-0.474 \pm i4.798}$ ($\boldsymbol{\xi = 9.84\%}$)	$\mathbf{-0.483 \pm i4.246}$ ($\boldsymbol{\xi = 11.30\%}$)

29. In this scenario, the proposed controller offers acceptable damping for the inter-area modes M5 and M6, whereas the ESS-based stabilizer [66] and WADC are less effective, as shown in Table 5.9. Similar results were obtained for most of the other modes of inter-area oscillations. Therefore, from the outcome presented in Table 5.9, we can infer that the proposed WADC provides robust damping of inter-area oscillation modes. Proposed controller is more effective not only for intact case but also under different contingencies.

Table 5.9: Damping performance of the study system under different contingencies

Operating conditions	**Fault location**	**Mode**	**ESS-based stabilizer [66]**	**WADC [61]**	**Proposed WADC**
OC1	Three-phase fault at the terminal of SG2	M1	$-0.402 \pm i4.940$ ($\xi = 8.11\%$)	$-0.423 \pm i4.731$ ($\xi = 8.9\%$)	$-0.448 \pm i3.978$ ($\xi = 11.19\%$)
		M2	$\mathbf{-0.293 \pm i4.536}$ ($\boldsymbol{\xi = 6.47\%}$)	$\mathbf{-0.368 \pm i4.027}$ ($\boldsymbol{\xi = 9.10\%}$)	$\mathbf{-0.433 \pm i3.942}$ ($\boldsymbol{\xi = 10.92\%}$)
OC2	Three-phase fault at the transmission line between Buses 4 and 14	M3	$-0.397 \pm i4.563$ ($\xi = 8.66\%$)	$-0.382 \pm i3.789$ ($\xi = 10.03\%$)	$-0.427 \pm i3.876$ ($\xi = 10.95\%$)
		M4	$\mathbf{-0.341 \pm i4.571}$ ($\boldsymbol{\xi = 7.44\%}$)	$\mathbf{-0.387 \pm i3.891}$ ($\boldsymbol{\xi = 9.89\%}$)	$\mathbf{-0.420 \pm i4.029}$ ($\boldsymbol{\xi = 10.38\%}$)
OC3	Three-phase fault at the transmission line between Buses 27 and 17 with line outage beteween Buses 28 and 29	M5	$-0.328 \pm i4.011$ ($\xi = 8.175\%$)	$-0.353 \pm i4.126$ ($\xi = 8.52\%$)	$-0.428 \pm i4.013$ ($\xi = 10.60\%$)
		M6	$\mathbf{-0.387 \pm i4.629}$ ($\boldsymbol{\xi = 8.33\%}$)	$\mathbf{-0.397 \pm i4.15}$ ($\boldsymbol{\xi = 9.52\%}$)	$\mathbf{-0.415 \pm i3.986}$ ($\boldsymbol{\xi = 10.35\%}$)

5.5 Validation on Real-Time Digital Simulator

The real-time verification of the proposed scheme is carried out on RTDS using the graphical user interface of RSCAD FX1.3. The workflow for real-time digital simulation is shown in Fig. 2.14 of chapter-2. The modified New England ten-machine benchmark system and BESS are modelled in the RSCAD draft using time steps of 50 μs in the mainstep and 3.333 μs in the substep interface, respectively. The IRIG-B signal is used to synchronize the GTSYNC card of the RTDS with a GPS clock. Also, the proposed WADC is simulated in NovaCor with the mainstep interface, which links the control signal to the BS1 active power control loop after receiving the measurement signal from the GTNET PMU of the simulator.

The following disturbances are simulated on the study test system to evaluate the WADC performance in different loading conditions.

- Disturbance 1 (DS1): At time t = 3 sec, a three-phase fault with a duration of 0.1 sec is applied at the terminal of SG2.
- Disturbance 2 (DS2): A three-phase fault is applied at the transmission line between buses 4 and 14 at t = 3 sec for 0.1 sec.
- Disturbance 3 (DS3): The outage of the transmission line between buses 28 and 29, in combination with a three-phase fault at t = 3 sec for 0.1 sec on the transmission line between buses 27 and 17.

The feedback control loop of WADC for BS1 has included the 200 ms communication latency in each disturbance simulation case.

5.5.1 Disturbance 1 (DS1)

The three-phase fault applied at the terminal of SG2 (i.e., bus 31) is simulated for the study system under operating condition OC1. Fig. 5.15 (a) and (b) show the dynamic responses of the inter-area tie-line P_{1-39} (Area-3 to Area-1) and P_{3-18} (Area-1 to Area-2). It is observed that the power oscillation through the two tie-lines are effectively damped under this fault, and the settling time and peak overshoot of power oscillation with proposed WADC is minimum compared to the ESS-based stabilizer scheme [66] and the WADC [61].

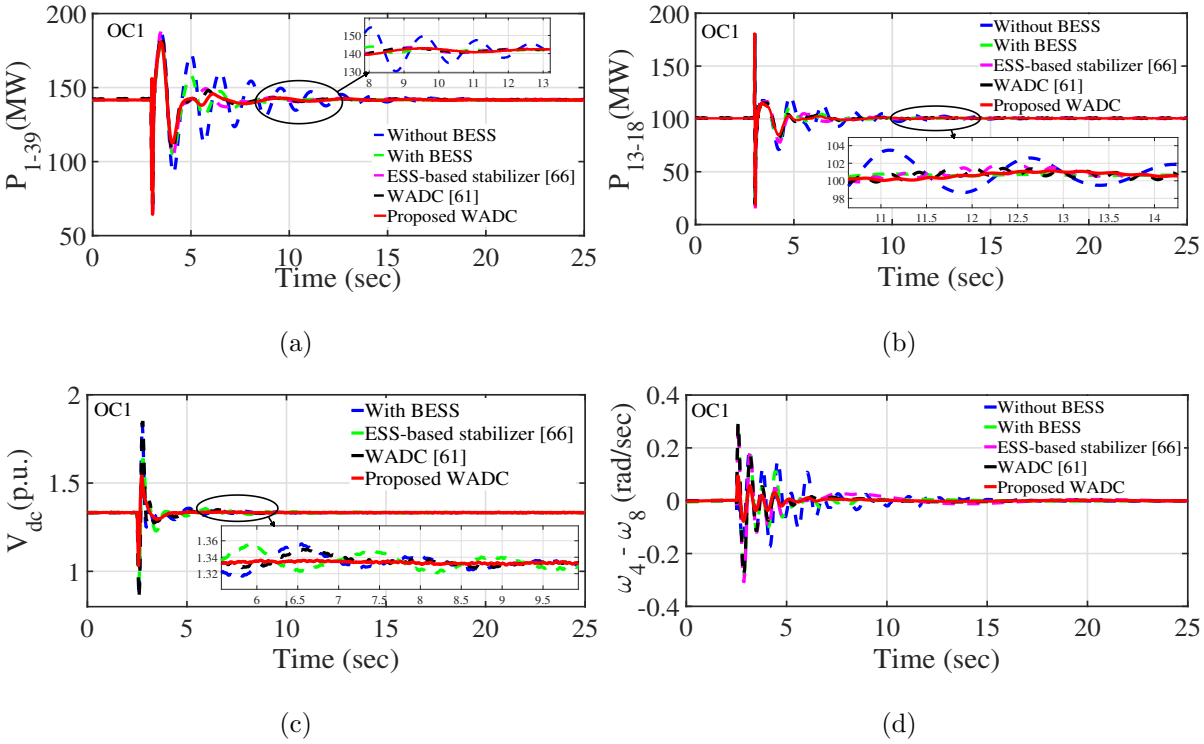

Figure 5.15: Dynamic simulation response of study test system with fixed communication delay of 200 ms under operating condition OC1. (a) Active power on line 1-39, (b) Active power on line 3-18, (c) BS1 converter DC-link voltage, and (d) Rotor speed deviation between SG4 and SG8.

Furthermore, Fig. 5.15 (c) depict the dynamic responses of the BS1 converter DC-link voltage. A better damping performance is achieved compared to ESS-based stabilizer [66] and WADC [61], which reveals the excellent damping capability of the proposed WADC

for BS1. The dynamic response of the rotor speed deviation between the SG4 and SG8 is shown in Fig. 5.15(d) to show that the proposed WADC has superior damping performance for prominent inter-area oscillation modes compared to existing ESS-based stabilizer [66] and WADC [61] control scheme.

5.5.2 Disturbance 2 (DS2)

The transmission line between buses 4 and 14 experienced a three-phase fault for 0.1 sec. Under operating condition OC2, the study system is simulated. The dynamic responses of the real power through lines P_{1-39} and P_{3-18} are shown in Fig. 5.16 (a) and (b). It can be seen that the power oscillation is better damped compared to an ESS-based stabilizer [66] and WADC [61]. The oscillation damping of the BS1 converter DC-link voltage is sufficiently damped too, as depicted in Fig. 5.16 (c).

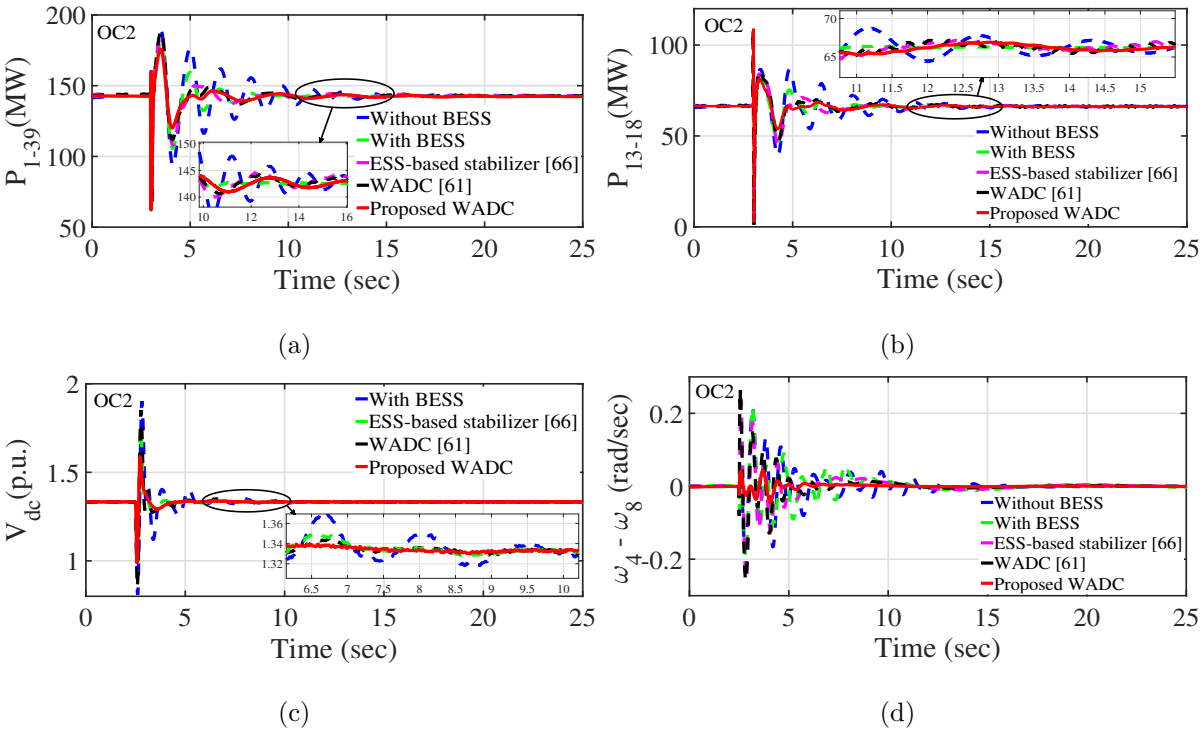

Figure 5.16: Dynamic simulation response of study test system with fixed communication delay of 200 ms under operating condition OC2. (a) Active power on line 1-39, (b) Active power on line 3-18, (c) BS1 converter DC-link voltage, and (d) Rotor speed deviation between SG4 and SG8.

Moreover, the difference in rotor speed between SG4 and SG8 is shown in Fig. 5.16 (d). It is clear that the proposed WADC settling time and peak overshoot of the SG

rotor speed deviation are less than those of the ESS-based stabilizer [66] and WADC [61] control scheme.

5.5.3 Disturbance 3 (DS3)

A three-phase fault is applied for 0.1 sec on the transmission line between buses 27 and 17, while the study test system's transmission line between Buses 28 and 29 is out. This simulation was performed under condition OC3. It can be seen that power flows across the inter-area tie-lines P_{1-39} and P_{3-18} are reduced due to the outage of the transmission line, as shown in Fig. 5.17 (a) and (b). It is observed further that the power oscillation on inter-area lines is more effectively damped than an ESS-based stabilizer [66] and WADC [61]. Also, the BS1 converter's DC-link voltage oscillation damping is significantly improved, as depicted in Fig. 5.17 (c). Additionally, as demonstrated in Fig. 5.17 (d), the proposed WADC successfully dampens the oscillation of rotor speed deviation between SG-4 and SG8 compared to ESS-based stabilizer [66] and WADC [61].

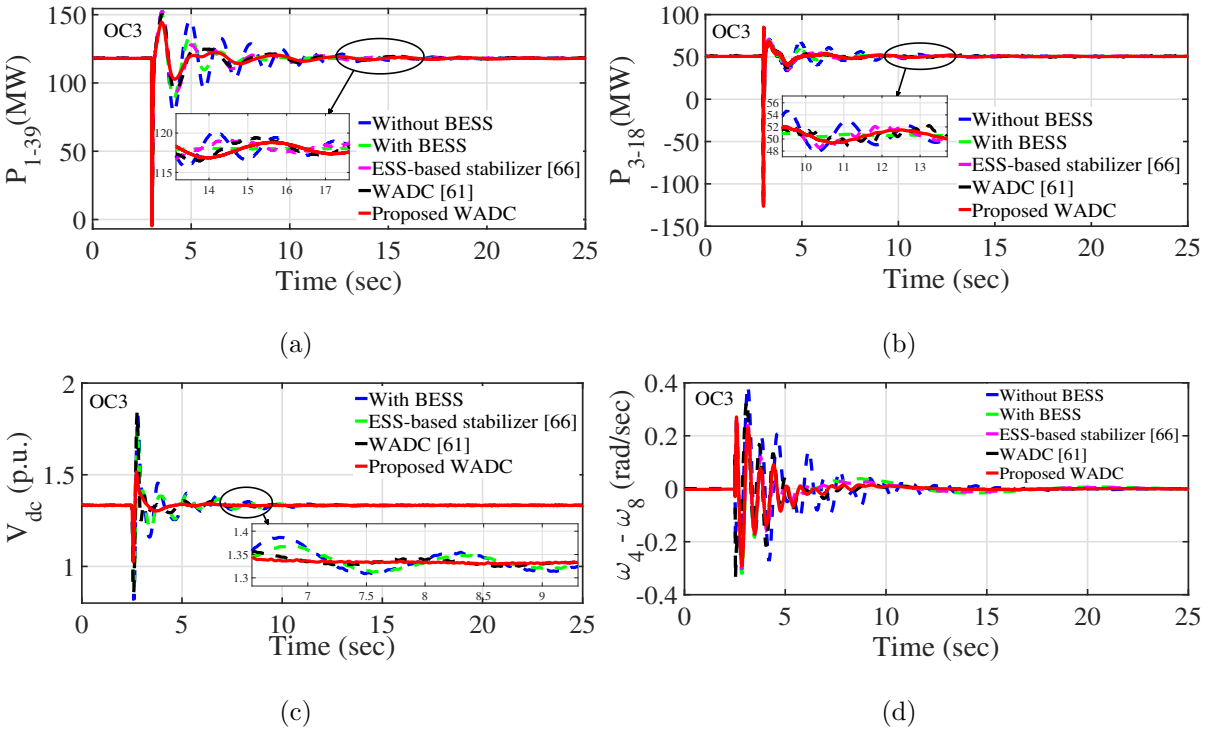

Figure 5.17: Dynamic simulation response of study test system with fixed communication delay of 200 ms under operating condition OC3. (a) Active power on line 1-39, (b) Active power on line 3-18, (c) BS1 converter DC-link voltage, and (d) Rotor speed deviation between SG4 and SG8.

According to the simulation outcomes, the proposed H_∞ mixed sensitivity scheme-based WADC for BS1 offers robust damping performance against various contingencies.

5.5.4 Control efficacy verification with the integration of renewable source

This study integrates a Doubly Fed Induction Generator (DFIG) based Wind Turbine System (WTS) into the New England ten-machine benchmark power system to assess the robustness and effectiveness of the proposed WADC scheme for BS1. The 150 MW power capacity of WTS is installed on bus-22. The WTS comprises 75 wind turbine generators (WTGs), each with a capacity of 2 MW, as shown in Fig. 5.18, which is a low inertia bus according to [98]. Also, a 150 MW capacity of an additional load is connected to this bus to maintain the load generation balance in this system (see Fig. 5.18). The data of WTG in simulation analysis is taken from [99], and the wind speed is considered 12 m/s in this analysis.

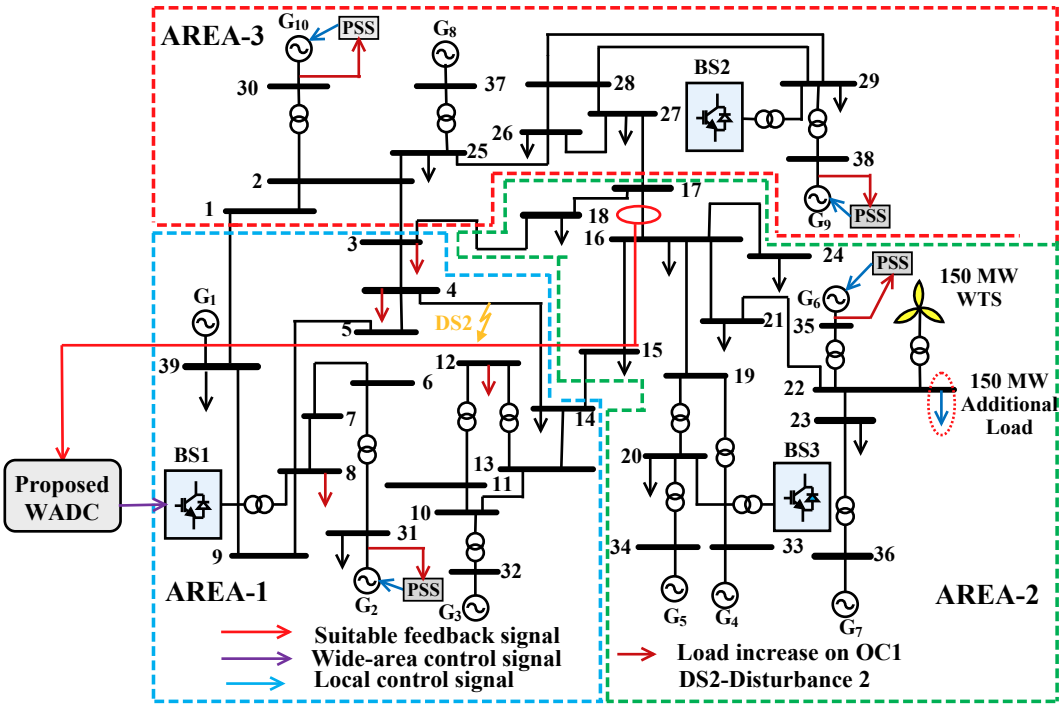

Figure 5.18: The 150 MW wind turbine system and a 150 MW additional load are added to the New England ten-machine system at bus 22.

The dynamics simulation analysis in the study system is performed under operating condition OC1, with the application of disturbance DS2. The dynamic response of the

rotor speed deviation between SG2 and SG5, as well as SG5 and SG9, are presented in Fig. 5.19 (a) and (b), respectively. It is evident that the rotor oscillation is effectively damped. The proposed WADC scheme's performance is superior to the ESS-based stabilizer [66] and WADC [61] control schemes regarding damping. The power flow across the line P_{1-39} depicted in Fig. 5.19 (c), demonstrated that the power oscillation along this line is efficiently damped under this scenario. Moreover, the DC-link voltage between the grid and the rotor side converter illustrated in Fig. 5.19 (d), shows that the oscillation in the DC-link voltage is adequately damped compared to the ESS-based stabilizer [66] and WADC [61] control schemes. Therefore, based on these dynamic simulation results, it is evident that the proposed WADC scheme for BS1 provides robust damping performance under renewable energy source penetration in the form of DFIG-based WTS.

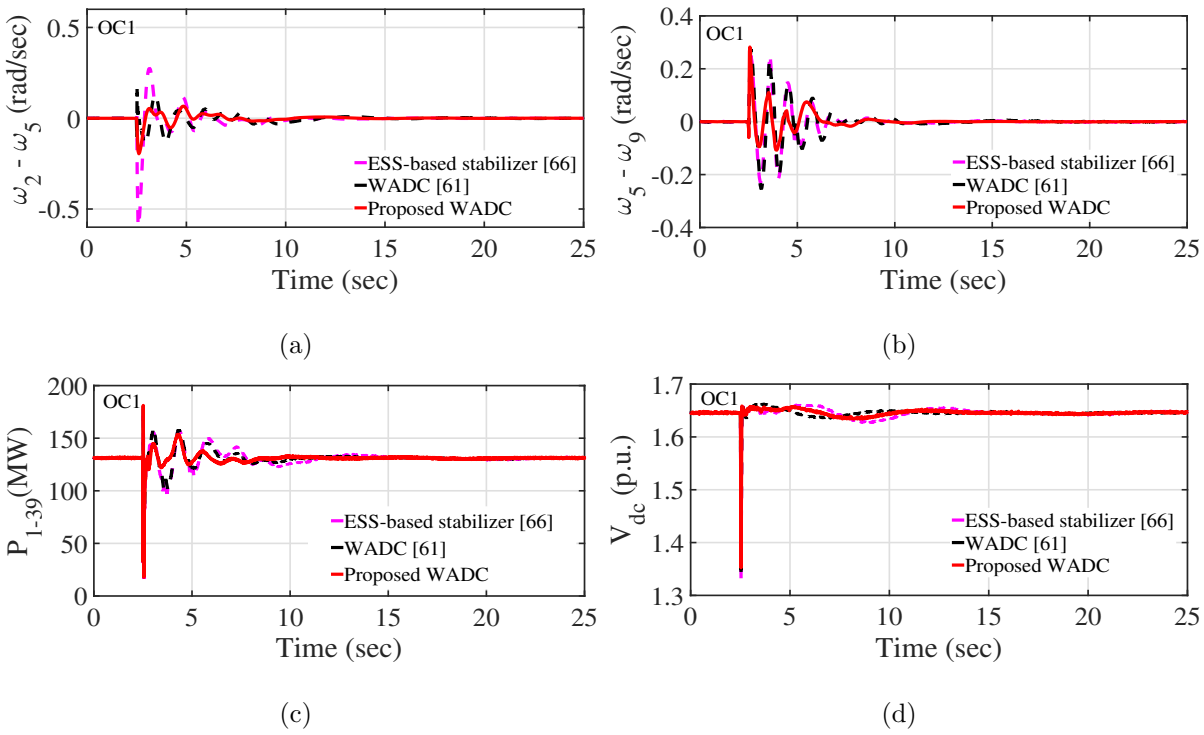

Figure 5.19: Dynamic simulation response of study test system with fixed communication delay of 200 ms as well as integration of WTS under operating condition OC1. (a) Rotor speed deviation between SG2 and SG5, (b) Rotor speed deviation between SG5 and SG9, (c) Active power on line 1-39, and (d) DC-link voltage between the grid and the rotor side converter.

5.5.5 Performance of WADC under variable communication time delay

The proposed control scheme with variable communication time delay is shown in Fig. 5.20. The impact of variable communication time delay on WADC damping performance for multi-machine power systems is discussed in [100]. Further modelling of variable communication time delay for WADC in the context of power system inter-area oscillation is suggested in [101]. The linearized state model of the power system with variable communication time delay is as follows:

$$\begin{cases} px_1(t) = Ax(t) + Bu(t) + A_\tau x_\tau(t-\tau_l) + B_\tau u_\tau(t-\tau_l) \\ y_1(t) = Cx(t) + Du(t) + C_\tau x_\tau(t-\tau_l) + D_\tau u_\tau(t-\tau_l) \end{cases} \tag{5.14}$$

where, τ is the variable communication time delay; $\tau_l = (\tau_1, \tau_2, ...\tau_{Nl})$ and $\tau_1 \neq \tau_2 \neq ... \neq \tau_{Nl}$; N_l is the total number of communication delay in the power system; A, B, C, and D are the matrix coefficients of the power system without communication delay, respectively; A_τ, B_τ, C_τ, and D_τ are the matrix coefficients of the power system with variable communication delay, respectively; x, x_τ, u and u_τ are the state and input vector of the system without and with variable communication delay, respectively.

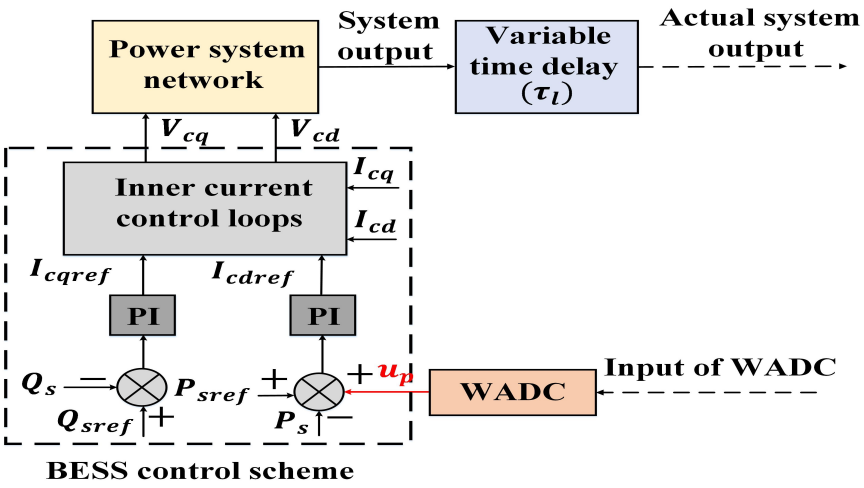

Figure 5.20: WADC for BESS with variable communication time delay.

In this work, the variable communication time delay ranging from 200 ms to 500 ms is considered, as depicted in Fig. 5.21. Further, τ_l is defined as follows [101]:

$$\tau_l = \bar{\tau}_l \pm \tau_l\left(\Delta\left(t_l\right)\right) \tag{5.15}$$

where, $\bar{\tau}_l$ and $\tau_l(\Delta(t_l))$ are the l^{th} mean value of the communication delay (i.e., constant delay), and the time-variant communication delay, which depends on t (i.e., total simulation time), respectively.

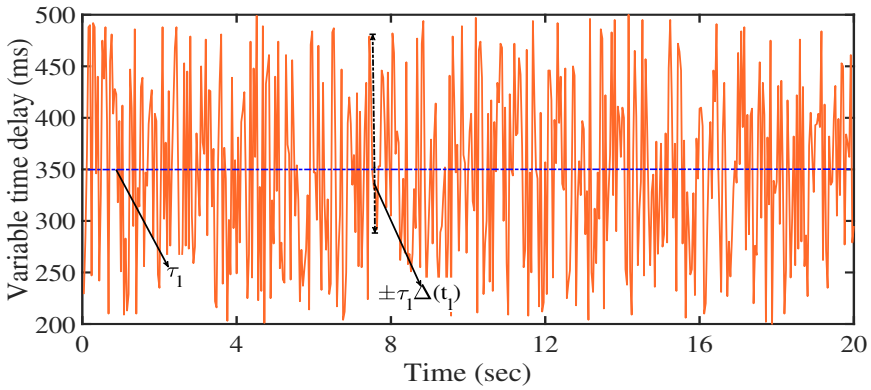

Figure 5.21: Variable communication time delay modelled using (5.15).

In this simulation analysis, we employed the variable communication time delay as shown in Fig. 5.21 in the feedback signal of the proposed WADC for BS1. This simulation case is conducted under two distinct operating conditions, OC2 and OC3, and are accompanied by disturbances DS2 and DS3, respectively. The dynamic simulation response of rotor speed deviation between SG4 and SG8 and SG2 and SG5 with proposed WADC as well as with ESS-based stabilizer [66] and with WADC proposed in [61],under the system operating conditions OC2 and OC3 are depicted in Fig. 5.22 and Fig. 5.23, respectively.

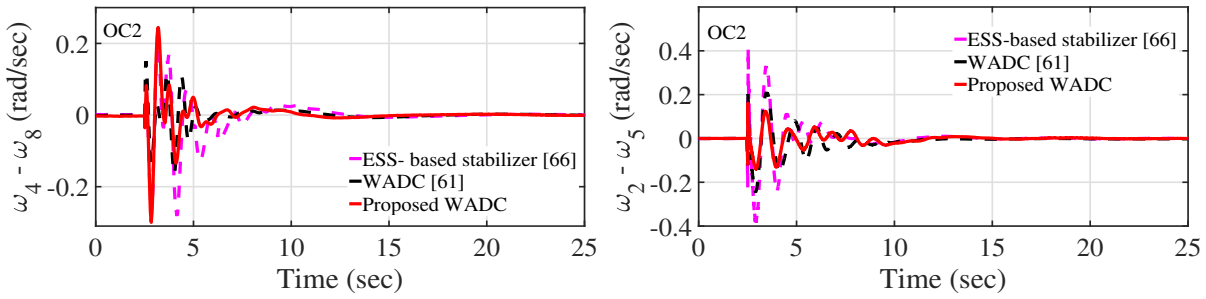

(a) (b)

Figure 5.22: Dynamic simulation response of study test system with variable communication delay under operating condition OC2. (a) Rotor speed deviation between SG4 and SG8, and (b) Rotor speed deviation between SG2 and SG5.

In the presence of variable communication time delay in the feedback signal, the rotor speed deviation between SG4 and SG8 is depicted in Fig. 5.22 (a) and Fig. 5.23 (a) under

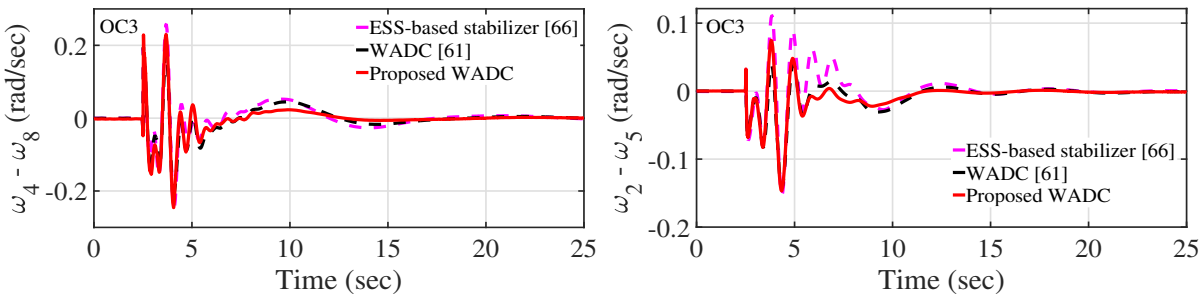

(a) (b)

Figure 5.23: Dynamic simulation response of study test system with variable communication delay under operating condition OC3. (a) Rotor speed deviation between SG4 and SG8, and (b) Rotor speed deviation between SG2 and SG5.

the operating conditions OC2 and OC3, respectively. Comparison of dynamic simulation response shown in Fig. 5.22 (a) with Fig. 5.16 (e) and Fig. 5.23(a) with Fig. 5.17 (e) shows that the rotor oscillation magnitude and settling time under variable communication delay are slightly higher compared to the case with fixed communication delay of 200 ms. However, the damping performance of the proposed WADC is better compared to the existing ESS-based stabilizer [66] and the WADC [61] when considering uncertainty associated with variable communication time delay.

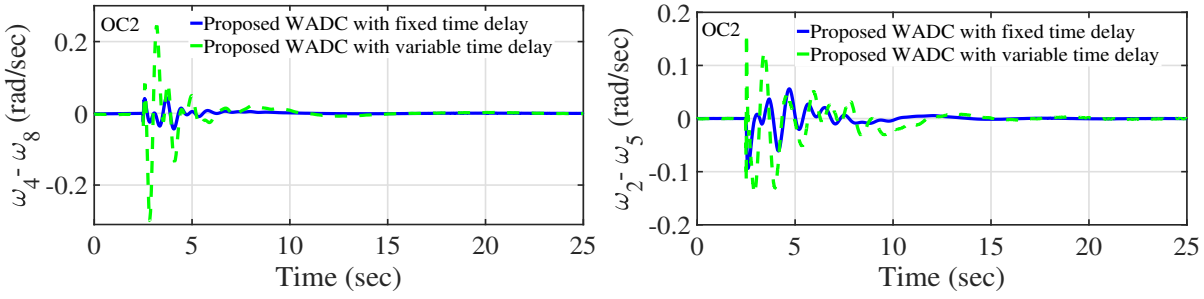

(a) (b)

Figure 5.24: Dynamic simulation response of the study test system with a proposed WADC, incorporating fixed and variable time delay, under operating condition OC2. (a) Rotor speed deviation between SG4 and SG8, and (b) Rotor speed deviation between SG2 and SG5.

Further, the dynamic simulation response of the study system with the proposed WADC employed with 200 ms fixed communication delay as well as with the variable communication delay under operating condition OC2 are shown in Fig. 5.24. Analysis of

the simulation response reveals that the proposed WADC, when equipped with a fixed communication delay in the feedback loop, provides better damping for inter-area oscillations in the system than employing variable communication delay. However, the proposed WADC effectively preserves system stability and provides robust damping performance under both variable and fixed communication time delays in the feedback signal.

5.6 Summary

This chapter presents the design of H_∞ mixed sensitivity scheme-based WADC for the BESS embedded power networks to alleviate inter-area modes. This controller offers robust damping performance for power system inter-area modes against changes in various operating conditions. From the modal analysis, this study observed that the power system inter-area oscillation modes are influenced not only by the close loop control mode interaction between SG and BESS but also by the change in system operating conditions. Also, the sensitivity to BESS control mode parameters affects the system's inter-area modes damping under the change in power system operating conditions. Furthermore, the proposed controller's superiority was evaluated through a comparison with the ESS-based stabilizer and an existing WADC. The real-time simulation outcomes verify the efficacy and superiority of the proposed WADC damping performance against power system prominent inter-area modes.